Figure 1.

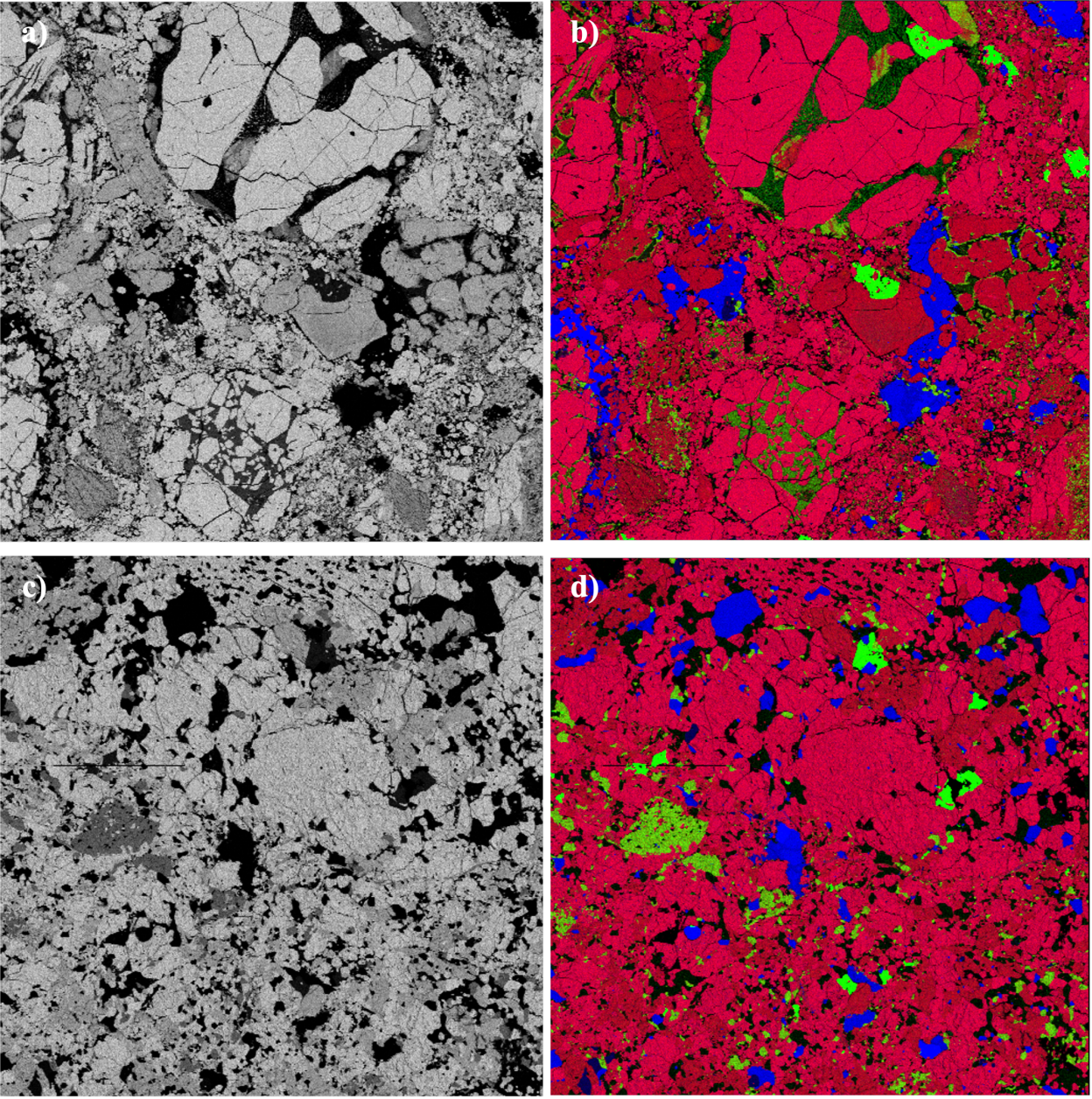
a)
b)
c)
d)

Figure 2.

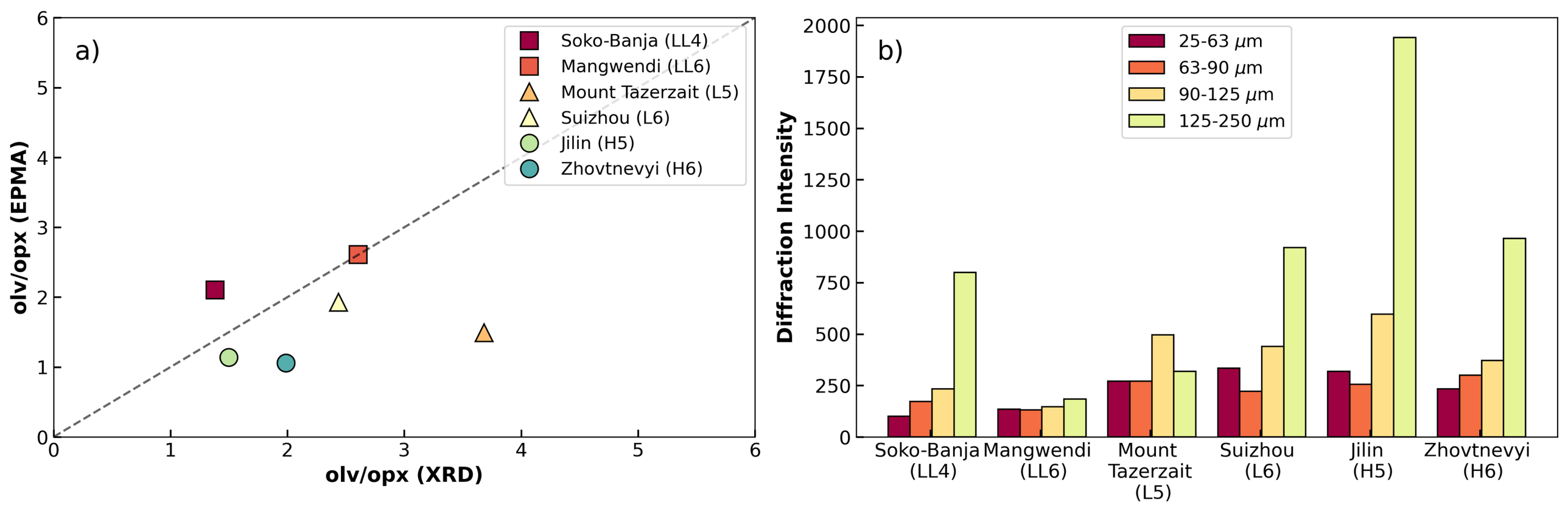
a)
Soko-Banja (LL4)
Mangwendi (LL6)
Mount Tazerzait (L5)
Suizhou (L6)
Jilin (H5)
Zhovtnevyi (H6)
olv/opx (EPMA)
olv/opx (XRD)
0
1
2
3
4
5
6
b)
25-63 μm
63-90 μm
90-125 μm
125-250 μm
Diffraction Intensity
0
250
500
750
1000
1250
1500
1750
2000
Soko-Banja (LL4)
Mangwendi (LL6)
Mount Tazerzait (L5)
Suizhou (L6)
Jilin (H5)
Zhovtnevyi (H6)

Figure 3.

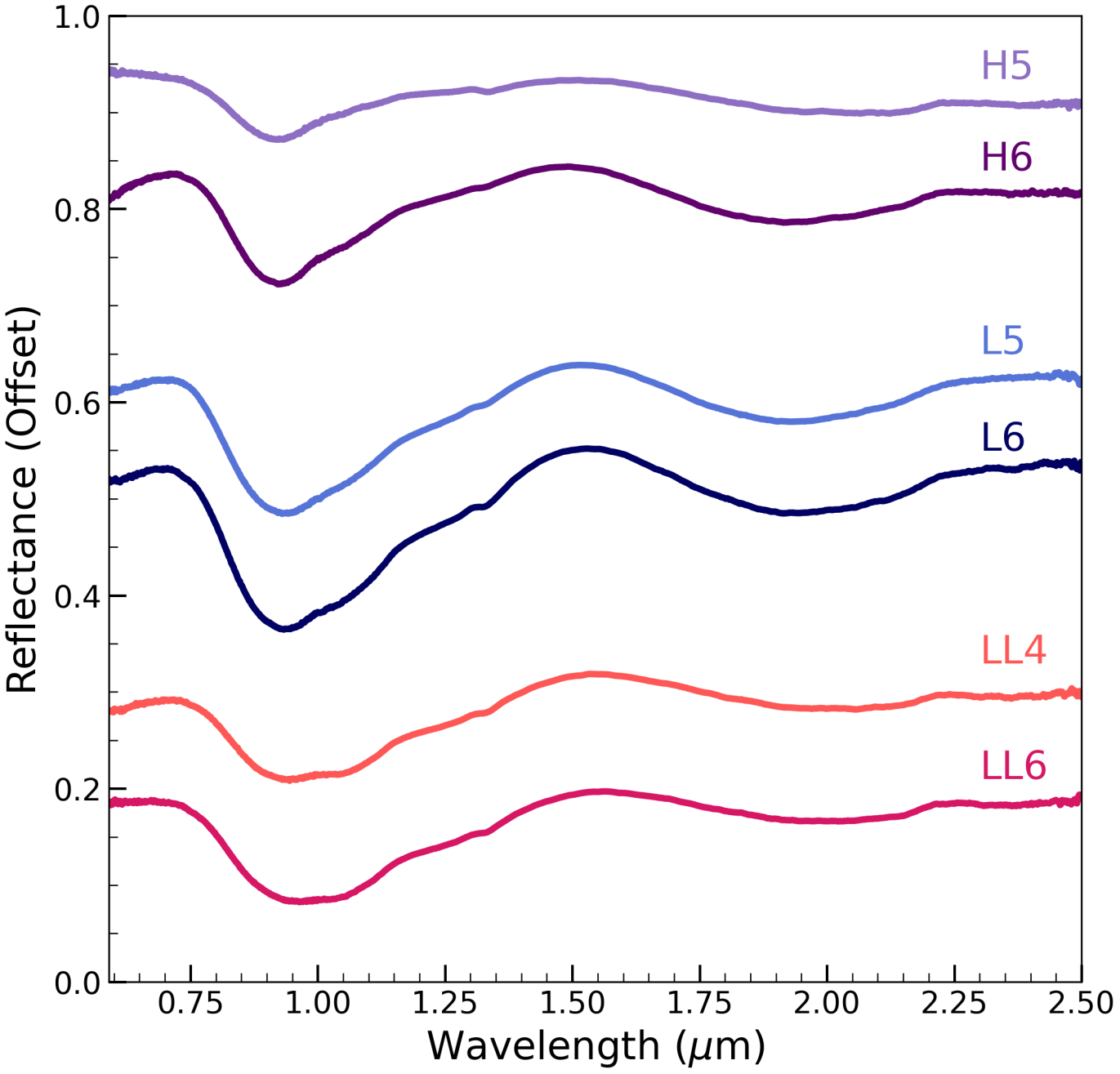
H5
H6
L5
L6
LL4
LL6
Reflectance (Offset)
Wavelength (μm)
1.0
0.8
0.6
0.4
0.2
0.0
0.75
1.00
1.25
1.50
1.75
2.00
2.25
2.50

Figure 4.

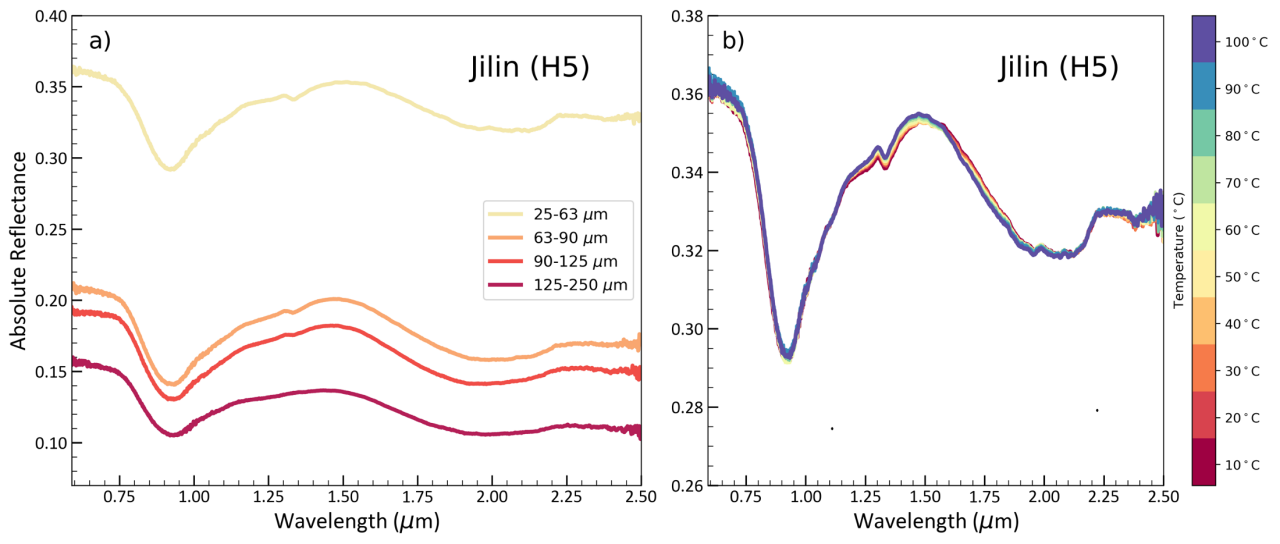
a)
Jilin (H5)
25-63 μm
63-90 μm
90-125 μm
125-250 μm
Absolute Reflectance
Wavelength (μm)
b)
Jilin (H5)
Wavelength (μm)
Temperature (°C)
100 °C
90 °C
80 °C
70 °C
60 °C
50 °C
40 °C
30 °C
20 °C
10 °C

Figure 5.

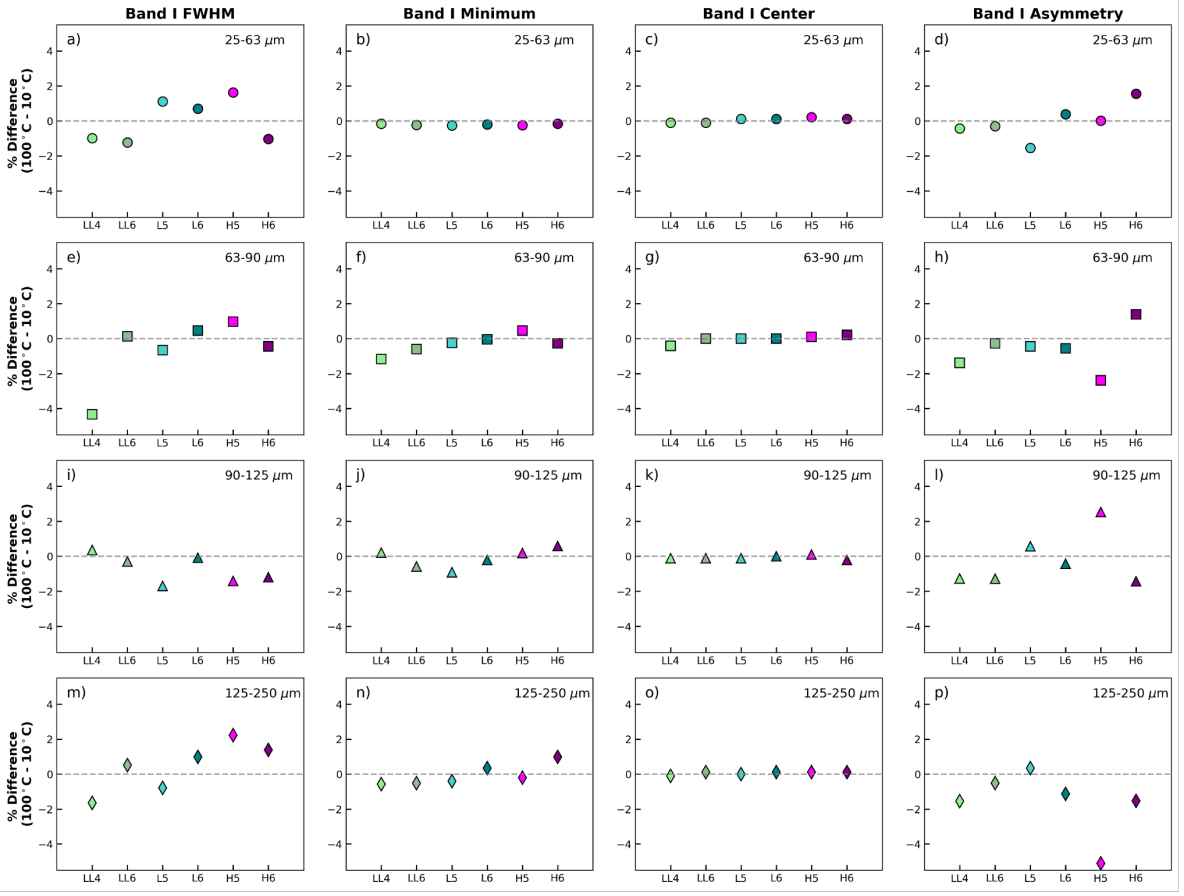
Band I FWHM
Band I Minimum
Band I Center
Band I Asymmetry
% Difference (100˚C - 10˚C)
a) 25-63 μm
b) 25-63 μm
c) 25-63 μm
d) 25-63 μm
e) 63-90 μm
f) 63-90 μm
g) 63-90 μm
h) 63-90 μm
i) 90-125 μm
j) 90-125 μm
k) 90-125 μm
l) 90-125 μm
m) 125-250 μm
n) 125-250 μm
o) 125-250 μm
p) 125-250 μm
LL4 LL6 L5 L6 H5 H6
4 2 0 −2 −4

Figure 6.

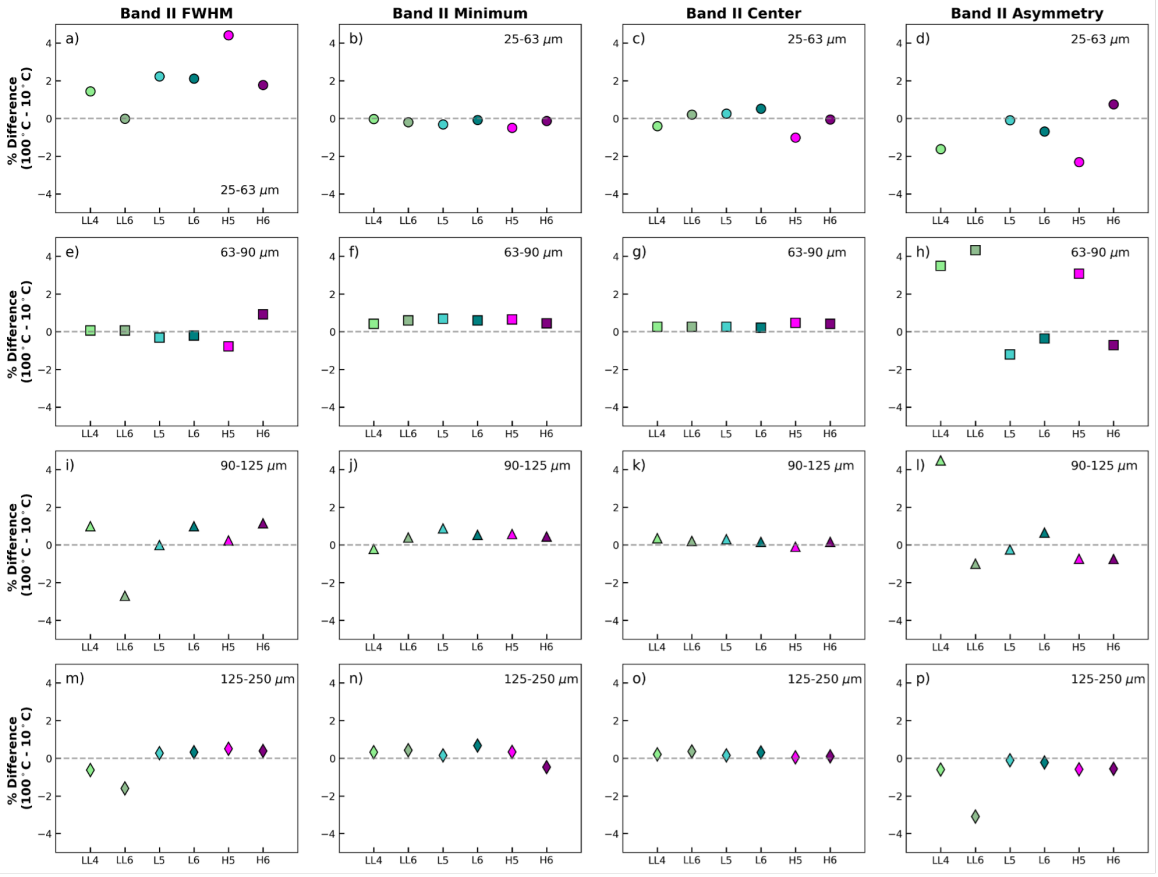
Band II FWHM
Band II Minimum
Band II Center
Band II Asymmetry
% Difference (100˚C - 10˚C)
a)
25-63 μm
b)
25-63 μm
c)
25-63 μm
d)
25-63 μm
e)
63-90 μm
f)
63-90 μm
g)
63-90 μm
h)
63-90 μm
i)
90-125 μm
j)
90-125 μm
k)
90-125 μm
l)
90-125 μm
m)
125-250 μm
n)
125-250 μm
o)
125-250 μm
p)
125-250 μm
LL4
LL6
L5
L6
H5
H6
4
2
0
−2
−4

Figure 7.

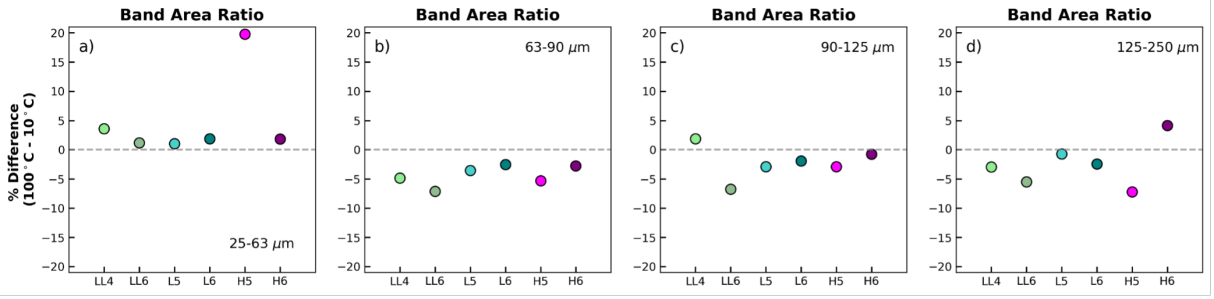
Band Area Ratio
a)
25-63 μm
b)
63-90 μm
c)
90-125 μm
d)
125-250 μm
% Difference
(100 °C - 10 °C)
20
15
10
5
0
−5
−10
−15
−20
LL4
LL6
L5
L6
H5
H6

Figure 8.

a)
b)
c)
d)
e)
f)
g)
h)
i)
j)
k)
l)
Band I FWHM
Band I Minima
Band I Center (μm)
Band I Asymmetry
25-63 μm
63-90 μm
90-125 μm
125-250 μm
Soko-Banja (LL4)
Mangwendi (LL6)
Mount Tazerzait (L5)
Suizhou (L6)
Jilin (H5)
Zhovtnevyi (H6)

Figure 9.

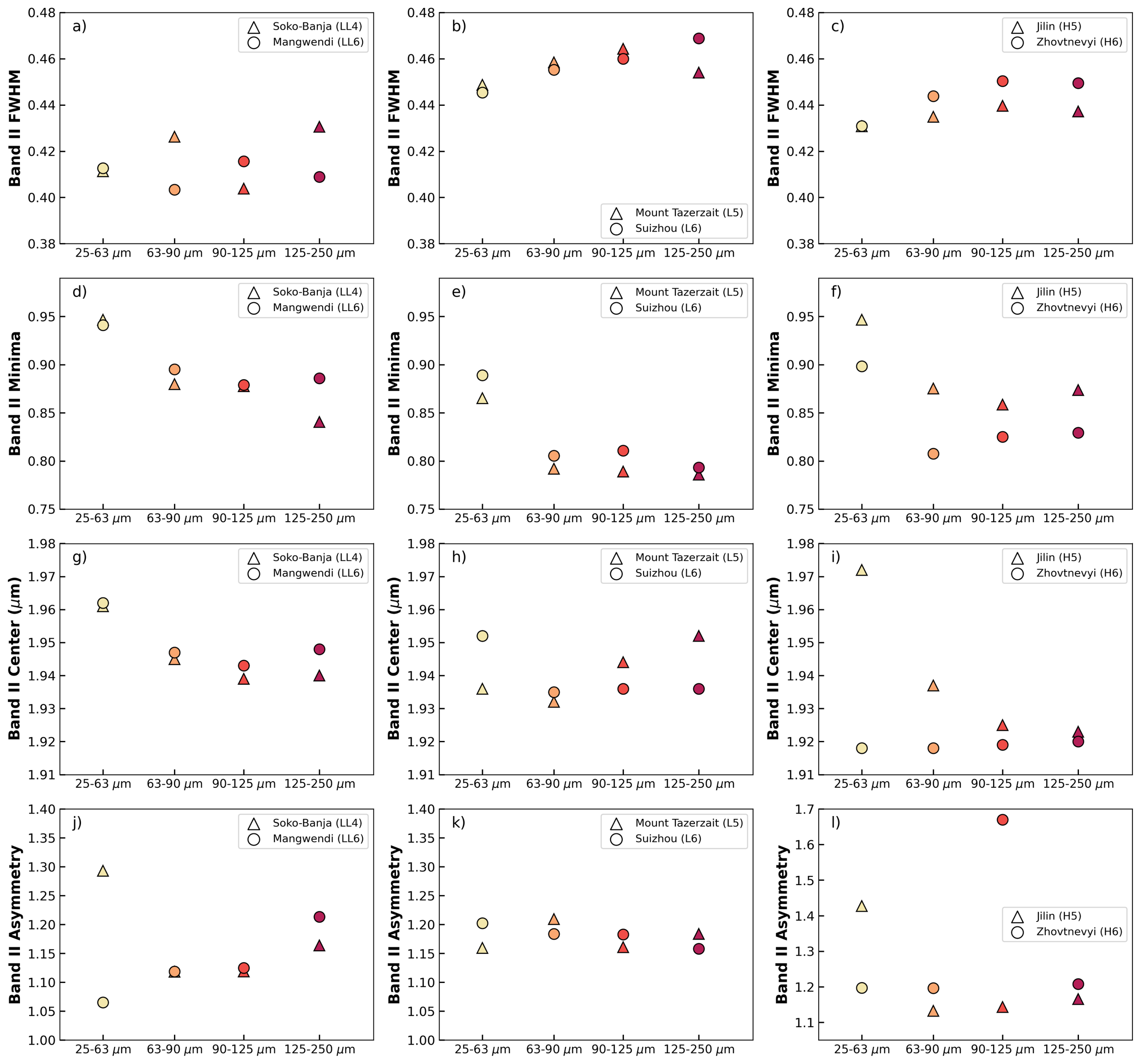
a)
b)
c)
d)
e)
f)
g)
h)
i)
j)
k)
l)
Soko-Banja (LL4)
Mangwendi (LL6)
Mount Tazerzait (L5)
Suizhou (L6)
Jilin (H5)
Zhovtnevyi (H6)
Band II FWHM
Band II Minima
Band II Center (μm)
Band II Asymmetry
25-63 μm
63-90 μm
90-125 μm
125-250 μm

Figure 10.

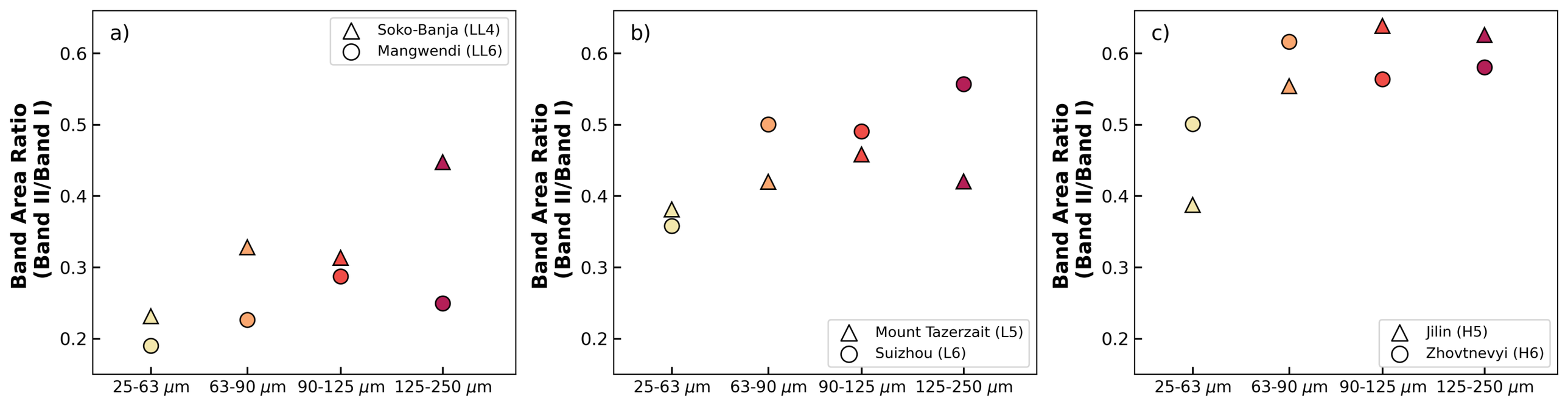
a)
Soko-Banja (LL4)
Mangwendi (LL6)
b)
Mount Tazerzait (L5)
Suizhou (L6)
c)
Jilin (H5)
Zhovtnevyi (H6)
Band Area Ratio
(Band II/Band I)
0.2
0.3
0.4
0.5
0.6
25-63 μm
63-90 μm
90-125 μm
125-250 μm

Figure 11.

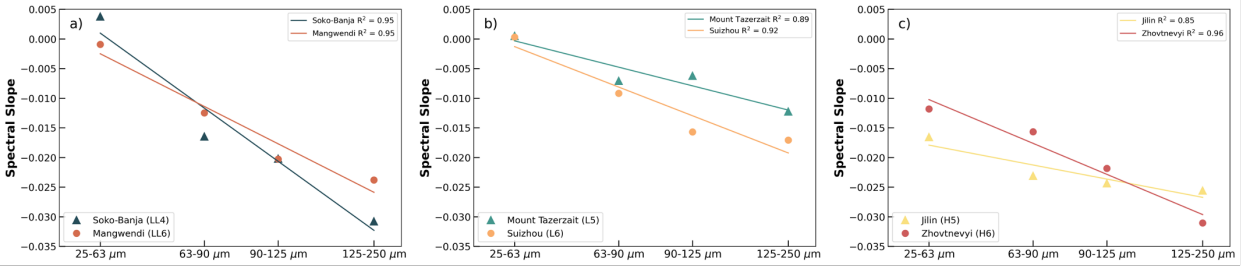
a)
b)
c)
Spectral Slope
0.005
0.000
−0.005
−0.010
−0.015
−0.020
−0.025
−0.030
−0.035
25-63 μm
63-90 μm
90-125 μm
125-250 μm
Soko-Banja R² = 0.95
Mangwendi R² = 0.95
Soko-Banja (LL4)
Mangwendi (LL6)
Mount Tazerzait R² = 0.89
Suizhou R² = 0.92
Mount Tazerzait (L5)
Suizhou (L6)
Jilin R² = 0.85
Zhovtnevyi R² = 0.96
Jilin (H5)
Zhovtnevyi (H6)

Figure 12.

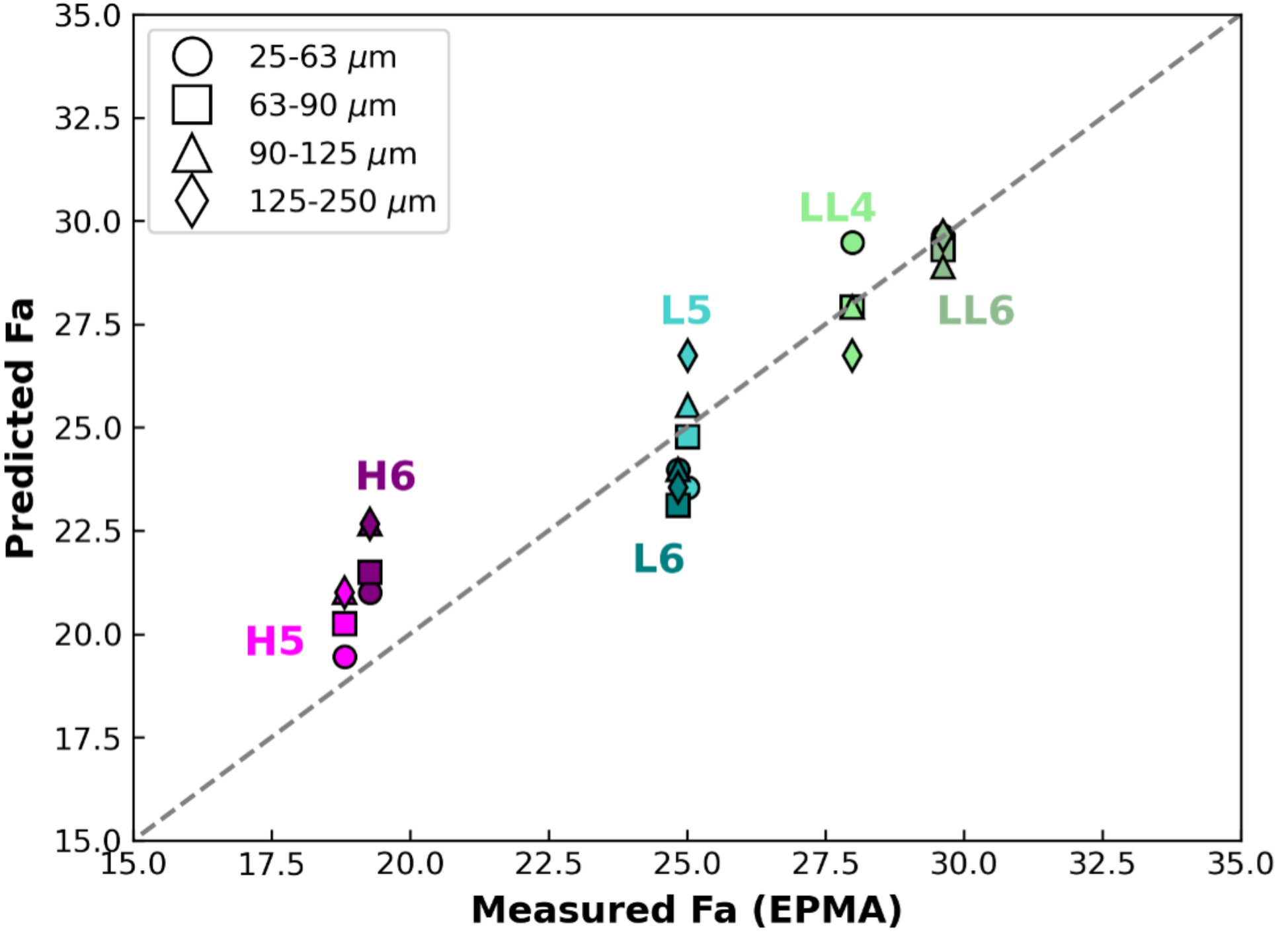
25-63 μm
63-90 μm
90-125 μm
125-250 μm
H5
H6
L6
L5
LL4
LL6
Predicted Fa
Measured Fa (EPMA)
35.0
32.5
30.0
27.5
25.0
22.5
20.0
17.5
15.0
15.0
17.5
20.0
22.5
25.0
27.5
30.0
32.5
35.0

Figure 13.

a)

25-63 μm
63-90 μm
90-125 μm
125-250 μm
LL chondrites (Dunn+2010c)
L chondrites (Dunn+2010c)
H chondrites (Dunn+2010c)

Band I Center (μm)

Band Area Ratio (Band II/Band I)

b)

From Dunn+2010c:
LL4 chondrite mean
LL6 chondrite mean
L5 chondrite mean
L6 chondrite mean
H5 chondrite mean
H6 chondrite mean

90-125 μm
Soko-Banja (LL4)
Mangwendi (LL6)
Mount Tazerzait (L5)
Suizhou (L6)
Jilin (H5)
Zhovtnevyi (H6)

Band I Center (μm)

Band Area Ratio (Band II/Band I)

c)

25-63 μm
63-90 μm
90-125 μm
125-250 μm
LL chondrites (Dunn+2010c)
L chondrites (Dunn+2010c)
H chondrites (Dunn+2010c)

Band I FWHM

Band I Asymmetry

d)

From Dunn+2010c:
LL4 chondrite mean
LL6 chondrite mean
L5 chondrite mean
L6 chondrite mean
H5 chondrite mean
H6 chondrite mean

90-125 μm
Soko-Banja (LL4)
Mangwendi (LL6)
Mount Tazerzait (L5)
Suizhou (L6)
Jilin (H5)
Zhovtnevyi (H6)

Band I FWHM

Band I Asymmetry

Effects of Particle Size, Temperature, and Metal Content on VNIR Spectra of Ordinary Chondrite Meteorites in a Simulated Asteroid Environment

Marina E. GEMMA[1,2,*], Katherine A. SHIRLEY[3], Timothy D. GLOTCH[1], Denton S. EBEL[2,4,5], Kieren T. HOWARD[5,6,2]

[1]Department of Geosciences, Stony Brook University, Stony Brook, NY, 11794, USA,
[2]Department of Earth and Planetary Sciences, American Museum of Natural History, New York, NY, 10024, USA,
[3]Atmospheric, Oceanic, and Planetary Physics, University of Oxford, Oxford OX1 3PU, UK,
[4]Lamont-Doherty Earth Observatory, Columbia University, Palisades, New York, NY, 10964, USA,
[5]Department of Earth and Environmental Sciences, Graduate Center of the City University of New York, New York, NY, 10065, USA,
[6]Department of Physical Sciences, Kingsborough College, City University of New York, Brooklyn, NY, 11235, USA

*Corresponding author: mgemma@amnh.org

Key Points:

1. Near-Earth asteroid temperatures (~10-100ºC) have a minimal effect on olivine and pyroxene dominated ordinary chondrite meteorite spectra.
2. Particle size is the most important variable to account for when trying to derive composition from remotely sensed asteroid VNIR spectra.
3. Metal content has a subtle but non-trivial effect on the VNIR spectra of ordinary chondrites.

Plain Language Summary

Remote interpretation of composition from asteroid spectra can be complicated by the physical (grain size, temperature) and chemical (mineral composition and abundance) properties of the asteroids themselves. To aid in understanding the effects of these variables and improve our remote interpretation of asteroid compositions, we have systematically evaluated the effects of these variables on the visible-near-infrared spectra of well-characterized ordinary chondrite meteorites measured in a simulated asteroid environment. Our results show that while the effect of near-Earth asteroid temperatures on the spectra appears to be minimal, changes in particle size can mimic changes in spectral band parameters that are typically attributed to composition. It is therefore essential to take particle size into account when interpreting composition from silicate-dominated asteroid spectra.

Abstract:

Laboratory spectral analysis of well-characterized meteorite samples can be employed to more quantitatively analyze asteroid remote sensing data in conjunction with returned extraterrestrial samples. In this work, we examine the combined effects of physical (temperature, particle size) and chemical (petrologic type, metal fraction) variables on VNIR spectra of ordinary chondrite meteorite powders. Six equilibrated ordinary chondrite meteorite falls were prepared at a variety of particle sizes to capture the spectral diversity associated with asteroid regoliths dominated by various grain sizes. Mineral compositions and abundance were determined from electron microprobe analysis of meteorite thick sections to precisely characterize changes in spectral features due to variations in mineralogy. VNIR spectra of the ordinary chondrite material were measured under simulated asteroid surface conditions at a series of temperatures chosen to mimic near-Earth asteroid surfaces. The resulting spectra show minimal variation in both major absorption bands across the simulated near-Earth asteroid temperature regime. Changes in particle size result in variations in band centers and band area ratios for material of the same composition, two key parameters typically used to derive asteroid composition. Unlike previous spectral investigations of ordinary chondrites, we retained the metal fraction in our powders instead of analyzing the silicate fraction only. Metal has a subtle but non-negligible effect on the VNIR spectra of ordinary chondrites. The more petrologically pristine samples from each ordinary chondrite group display relatively weaker absorption bands than their more thermally altered counterparts. The band centers shift to longer wavelengths as temperature, grain size, and petrologic type increase.

1 Introduction

Establishing strong links between the plethora of meteorite samples in collections on Earth and the parent body asteroids they originated from is a valuable outcome of past (NEAR-Shoemaker, Hayabusa, Hayabusa2, Dawn) and present (OSIRIS-Rex, Lucy, Psyche) space missions. Asteroid sample return missions (Hayabusa, Hayabusa2, OSIRIS-REx) provide much needed context for the study of relevant extraterrestrial samples already on Earth in the form of meteorites (Nakamura et al., 2011; Yokoyama et al., 2022; Lauretta et al., 2024). By utilizing these specimens of asteroids in the laboratory, it is possible to supply detailed chemical, mineralogical and petrological information for reference libraries of materials relevant to asteroid missions (Bates et al., 2020; Dunn et al., 2010).

NASA's OSIRIS-REx and JAXA's Hayabusa2 missions visited small near-Earth asteroids (NEA) thought to be similar in composition to carbonaceous chondrites (Lauretta et al., 2022; Ito et al., 2022), while the previous NEAR-Shoemaker and Hayabusa missions visited asteroids with compositions similar to that of ordinary chondrite meteorites (Trombka et al., 2000; Nakamura et al., 2011). JAXA's initial Hayabusa mission to asteroid 25143 Itokawa was the first to return samples from an asteroid and was able to directly link Itokawa to the LL-group ordinary chondrites (Nakamura et al., 2011), which was fundamental in validating the relationship between meteorite mineralogy and remotely sensed asteroid spectra of space-weathered bodies. This ground-truthing is an indispensable tool, enabling direct correlation of remotely sensed data with actual samples from the same asteroids, which can in turn help improve interpretation of spectra from unsampled asteroids.

This direct compositional link between remote asteroid observations and returned samples becomes even more consequential when considering that physical properties of asteroids can add significant complexity to remote spectral analysis of them. Both temperature and regolith grain size are variable on asteroid surfaces and are known to influence the diagnostic

spectral features that are used to determine asteroid compositions in both the near-infrared (NIR) and mid-infrared (MIR) wavelengths. It can therefore become difficult to decipher asteroid surface compositions if the physical properties of these airless small bodies are complicating interpretation of their spectra.

The spectral effects of these properties can be appropriately constrained through relevant laboratory spectral analysis of meteorite samples. Here we scrutinize the combined effects of temperature, particle size, and compositional differences on the visible and near-infrared (VNIR) spectral parameters of well-characterized ordinary chondrite meteorites. The results of this laboratory analysis can be applied to more quantitatively analyze asteroid remote sensing data in conjunction with returned samples, and more accurately determine the metal content on purportedly metal-rich bodies such as asteroid 16 Psyche.

2 Background

2.1 Ordinary Chondrite Meteorites

Ordinary chondrites comprise the bulk of meteorite collections, representing ~80% of all observed meteorites to fall (Hutchison, 2004). Though they represent a biased sampling of the material in the asteroid belt (Gaffey et al., 1989; McSween et al., 1991, Heck et al., 2004, Vernazza et al., 2008), their abundance on Earth renders them a useful sample pool for comprehensive spectral studies.

The ordinary chondrites are split into three chemically homogeneous groups: H (high total Fe), L (low total Fe), and LL (low total Fe, low metallic Fe) (Urey and Craig 1953; Van Schmus and Wood 1967; Rubin, 1990). These groups are distinguishable by characteristics such as chondrule size (Friedrich et al., 2015), which increases from H (0.3 mm) to LL (0.9 mm), metal abundance, which decreases from H (8 vol%) to LL (2 vol%), and Fe-rich olivine abundance, which increases from H (16-20 mol%) to LL (27-32 mol%; Weisberg et al., 2006). Meteorites that straddle group boundaries are classified as intermediate (e.g., L/LL, H/L).

Within each group, individual meteorites are assigned their own petrologic type. A petrologic type of 3.0 indicates that a meteorite is pristine, or that it experienced essentially no alteration. Petrologic types above 3 (3.1 to 6) signal increasing degrees of thermal metamorphism, resulting in chemical equilibration and recrystallization for types 4 and above. Types 2 to 1 represent increasing degrees of aqueous alteration. The ordinary chondrites span petrologic types 3 to 6, and each meteorite is designated by a combination of its group and petrologic type (e.g., H5). Though rare, petrologic type 7 ordinary chondrites have been identified (Weisberg et al., 2006), but are not considered for this study. Olivine composition is a primary indicator of metamorphic grade (Van Schmus and Wood 1967; Huss et al., 2006). Content of fayalite (Fa, Fe_2SiO_4), the Fe-rich endmember of the olivine solid solution series $(Mg,Fe)_2SiO_4$, is highly variable in the unequilibrated (type 3) ordinary chondrites, but converges to a consistent value for equilibrated (type 4-6) ordinary chondrites of each group. The content of ferrosilite (Fs, $FeSiO_3$), the Fe-rich endmember of low-Ca pyroxene $(Mg,Fe)SiO_3$, is not as sensitive as Fa to metamorphic alteration, but does tend to increase as equilibrated petrologic type increases (Dodd et al., 1967,1969; Huss et al., 2006). Furthermore, Fe-Ni metal alloy exsolves into Ni-rich (taenite) and Ni-poor (kamacite) phases, sulfide grain size notably increases, and minor mineral phases such as Ca-phosphate and chromite exsolve from chondrule phases as metamorphism increases (Grossman and Brearley 2010; Jones et al., 2014).

The compositions of ordinary chondrite meteorites are well studied (Mason 1963; Dodd et al., 1967; Kallemeyn et al., 1989; Jarosewich 1990; Dunn et al., 2010a,b). Olivine and low-Ca pyroxene are the most modally dominant phases, typically followed by high-Ca pyroxene

(CaMgSi$_2$O$_6$), anorthite-normative chondrule mesostasis, troilite (FeS), Fe-Ni metal (kamacite and taenite), and other minor phases (e.g., Ca-phosphate, chromite). However, these meteorites exhibit mineral proportions that are highly variable, dependent on petrologic type, and the result of differing parent body processes (Rubin, 2005b; Jones et al., 2014). Mineralogy varies even within the same petrologic type of the same ordinary chondrite group (McSween et al., 1991).

When using meteorites to derive relationships between spectral parameters and composition, it is therefore crucial to precisely characterize the individual ordinary chondrite meteorites used in the analysis rather than rely on the average properties of a particular meteorite group or petrologic type. If trying to constrain small differences in spectral features, it is necessary to ensure observed variations are not due to compositional differences given the highly variable mineralogies in ordinary chondrite samples.

2.2 Meteorite-Asteroid Relationships

Though meteorites and asteroids are unquestionably linked, they are classified based on different schemes. Determining the mineralogy, petrology, whole-rock chemistry, and oxygen isotope characteristics of a meteorite sample is normally necessary to properly place it in the meteorite classification system (Weisberg et al., 2006). This is feasible for the extraterrestrial materials present on Earth but is nearly impossible to achieve for remotely analyzed asteroid parent bodies. As a result, spectroscopic observations of asteroids rely on a separate scheme, splitting asteroids into spectral classes, with the most recent taxonomy establishing 24 classes via principal component analysis of VNIR asteroid spectra (Bus and Binzel, 2002; DeMeo et al., 2009). Efforts to place meteorite spectra into the Bus-DeMeo asteroid taxonomy have shown that meteorites do not fit neatly into asteroid spectral classifications, and that the spectral range of meteorites is likely broader than that of observed asteroids (Burbine et al., 2024). Other efforts have utilized machine learning technology to make the link between asteroid and meteorite classification more explicit (Dyar et al., 2023).

The only meteorites to be definitively linked to an asteroid thus far are the LL-group ordinary chondrites, shown to be chemically identical to particles returned from JAXA's initial Hayabusa mission to asteroid 25143 Itokawa (Nakamura et al., 2011) and the CI chondrites, shown to be isotopically related to returned samples from the Hayabusa2 mission to asteroid 162743 Ryugu (Greenwood et al., 2023). Ground-based (Binzel et al., 2001) and spacecraft-based (Abe et al., 2006; Okada et al., 2006) observations of asteroid Itokawa prior to sample return suggested that its surface composition was consistent with LL5 or LL6 chondrites, which was confirmed when analysis of returned particles displayed a mixture of equilibrated and "less-equilibrated" LL chondrite materials (Tsuchiyama et al., 2011).

Determining properties of asteroids with enough detail to definitively link them to a particular meteorite group may be possible via visiting spacecraft (e.g., Dawn at Vesta; De Sanctis et al., 2013, Rousseau et al., 2021), but even so, constraining the spectral features and variations of well-characterized meteorite samples in the laboratory is the more accessible and economical option to more precisely link asteroid classes to specific meteorite groups and vice versa.

2.3 VNIR Reflectance Spectroscopy

2.3.1 Mafic Mineralogies and VNIR Spectral Features

Reflectance spectroscopy is particularly well suited for determining mineralogies relevant to ordinary chondrite meteorites due to the presence of diagnostic spectral features of olivine and pyroxene in the VNIR. The spectral properties of the olivine- and pyroxene-rich ordinary chondrites and S-type asteroids are dominated by absorption bands located near wavelengths of 1 μm and 2 μm (called Band I and Band II, respectively). These absorption bands are caused by

188 the electronic and crystal field transitions of Fe^{2+} in the M1 or M2 crystallographic sites of these
189 mafic silicate minerals (Adams, 1974, 1975; Burns, 1993). The 1 μm olivine feature is a
190 composite of multiple overlapping absorption bands, and its wavelength position (band center)
191 shifts to longer wavelengths as iron content in olivine increases (Singer, 1981; Burns, 1993;
192 Sunshine and Pieters, 1998). Olivines with high iron content ($<Fo_{30}$) were observed to produce
193 larger band widths by Sunshine and Pieters (1998). Pyroxenes have absorption features at both 1
194 μm and 2 μm, and the band centers also shift to longer wavelengths as iron content increases in
195 the low-Ca pyroxenes (Burns et al., 1972; Cloutis and Gaffey, 1991). A correlation between band
196 position and composition of the high-Ca pyroxenes has been observed for some pure mineral
197 samples (Cloutis and Gaffey, 1991; Klima et al., 2011), but no such correlation was found to
198 exist for high-Ca pyroxene in ordinary chondrites (Dunn et al., 2010c).
199 The multi-mineralic ordinary chondrites were first thoroughly spectrally investigated by
200 Gaffey (1976), who emphasized that the relative abundance of the mineral phases does not
201 directly correlate with apparent spectral abundance; rather, that the relative optical density of a
202 mineral phase is the most important determinant in the relative spectral contribution of a mineral
203 phase. In other words, the phase with the highest optical density will be the greatest contributor
204 to the spectral character of a multi-mineralic material – for ordinary chondrites, this phase is
205 pyroxene. Gaffey (1976) also concluded that the band positions (centers) of the 1 μm and 2 μm
206 absorption features are indicative of pyroxene compositions and of the olivine/pyroxene ratio.
207 The diagnostic absorption features of pure minerals are reflected in multi-mineralic
208 samples, but deconvolving the relative contributions of these minerals, particularly for samples
209 such as ordinary chondrites with at least nine distinct mineral phases, is complex (Gaffey, 1976;
210 Sunshine et al., 1990; Sunshine et al., 1993) and requires knowledge of the optical constants of
211 the constituent phases and a radiative transfer-based spectral analysis model, such as those
212 proposed by Hapke (1981) or Shkuratov et al. (1999).
213 *2.3.2 Physical Effects on VNIR Spectra*
214 The interpretation of remotely sensed asteroid spectra is complicated by the known
215 effects of temperature and grain size on near-infrared spectral properties of minerals (Singer and
216 Roush, 1985; Roush and Singer, 1986; Moroz et al., 2000), meteorites, asteroids, and lunar
217 materials (Lucey et al., 1998, 2002; Hinrichs and Lucey, 2002). The surface temperatures of
218 asteroids vary, depending on properties such as orbit, inclination, incident solar radiation, and
219 composition, as do the grain sizes present on asteroid surfaces. Additionally, because asteroids
220 are airless bodies, their surfaces experience steep temperature gradients in the upper layers of
221 regolith. This effect is particularly relevant when considering VNIR spectra, since reflectance
222 spectroscopy is only concerned with the upper few microns of surface regolith.
223 *2.3.2.1 Effects of Temperature on VNIR Spectra*
224 Temperature has been shown to have a strong effect on the VNIR spectral features of
225 pure mafic silicate minerals such as olivine and pyroxene. Measurements over the temperature
226 range 80-448 K completed by Roush and Singer (Singer and Roush, 1985; Roush and Singer,
227 1986) revealed multiple changes in spectral features due to temperature. In the 1 μm olivine
228 band, they observed changes in absorption strength (band minimum) with changes in
229 temperature, but no significant wavelength shift of the band center. For the pyroxenes (low-Ca
230 and high-Ca pyroxene), they observed strong changes in band symmetry due to temperature,
231 with the longer wavelength edge shifting the most. The 1 μm pyroxene band did not show
232 changes in the wavelength position of the reflectance minima with changes in temperature, but
233 the 2 μm pyroxene band did. For low-Ca pyroxene, the 2 μm band shifts to higher wavelengths

with increased temperature, though for high-Ca pyroxene, the band shifts to shorter wavelengths with increased temperature (Singer and Roush 1985; Roush and Singer 1986). Later work on the same minerals confirmed these observations (Hinrichs, 1999; Hinrichs and Lucey, 2002).

The importance of accurately simulated environmental conditions for laboratory measurements was emphasized by Moroz et al. (2000), who demonstrated that the spectra of the olivine-rich A-type asteroids only corresponded to spectra of olivine at low temperatures, not at ambient terrestrial conditions. The unique thermal environments of airless body regoliths thus require precise simulation to fully understand associated spectral variations (Shirley and Glotch, 2019).

To first order, chondritic meteorites are mixtures of the mafic silicate minerals olivine and pyroxene. Understanding the spectral dependence on temperature for both mineral and meteorite powders is necessary, as VNIR spectra of meteorite powders cannot necessarily be treated as simple linear mixtures of minerals. In contrast to the pure minerals discussed above, temperature has a demonstrably smaller effect on VNIR spectra of multi-mineralic powders, such as lunar and meteoritic samples. Hinrichs and Lucey (2002) determined that spectral variations due to changes in temperature are much smaller for the 1 μm absorption feature of a multi-mineralic ordinary chondrite powder than for the 1 μm absorption feature for pure forsterite. Sanchez et al. (2012) found that the 2 μm absorption feature was most affected by temperature variations, noting shifts in Band II centers to longer wavelengths and a decrease in Band II depth as temperature increases, as well as a negative correlation between the ratio of band areas (Band II area/Band I area) and temperature.

2.3.2.2 Effects of Grain Size on VNIR Spectra

Grain size has been shown to have a similarly strong effect on VNIR spectral features of pure minerals because it controls the amount of light scattered and absorbed by a grain (Clark and Roush, 1984; Hapke, 2012). As grain size increases, the overall reflectance decreases, while the depth of absorption increases, reaches a maximum, then decreases (Clark, 1999). More negative (bluer) spectral slopes are also expected for larger grain sizes (Reddy et al., 2015).

For the mixtures of olivine and low-Ca pyroxene examined by Cloutis et al. (1986), the band area ratio (BAR) and the Band I center were shown to be generally independent of particle size. When the compositions of the mineral phases were known, they were able to use the spectral albedo in the 0.6 to 0.7 μm region to constrain particle size because it is insensitive to phase abundance. Analysis of pyroxene mixtures in Sunshine et al. (1993) revealed that band centers, widths, and relative strengths of absorptions from individual pyroxenes in the spectra of mixtures are independent of particle size. Other studies of particle size effects on VNIR spectra of mineral mixtures (Martian analog materials by Cooper and Mustard, 1999; HED meteorites by Cloutis et al., 2013) observed that increasing grain size causes band depths and widths to increase, and Cloutis et al. (2013) noted that for the largest grain sizes used (90-250 μm and 250-500 μm), the reflectance can remain unchanged, and the band depths may eventually decrease with increasing grain size.

2.3.2.3 Effects of Phase Angle on VNIR Spectra

Another non-chemical variable that can affect spectral band parameters used for compositional determination is phase angle. Phase angle refers to the angular separation between the illumination source (e.g., the Sun) and the observer (e.g., spacecraft instrument) as seen from the target (e.g., an asteroid). For VNIR spectra, changes in phase angle for different measurements can result in a more positive spectral slope (reddening) and variations in albedo and absorption band depth (Clark et al., 2002; Sanchez et al., 2012). Small variations in band

centers and band area ratio (BAR) values were also observed for varying phase angles of the target NEAs by Sanchez et al. (2012).

2.4 Motivation

Given that grain size and temperature have been individually shown to have effects on the spectral features of powdered samples, the goal of this work was to determine how the combined effects of temperature, grain size, and compositional differences between petrologic types and across ordinary chondrite groups influence VNIR spectral features at simulated asteroid surface conditions. Ordinary chondrite meteorites were chosen for investigation not only because the LL chondrites are definitively linked to an asteroid, but also because their prevalence in collections enabled assembly of a large sample suite that could be thoroughly characterized both mineralogically and petrologically to better understand how the aforementioned variables affect spectral features. Unlike previous spectral investigations of the ordinary chondrites that removed the metal fraction from the meteorite powder (e.g., Dunn et al., 2010c), this coordinated mineralogical, compositional, and spectral study of ordinary chondrite meteorites retained the metal in ordinary chondrite meteorite powders to more realistically represent asteroid regolith compositions, in an effort to enable better compositional and physical characterization of asteroids with metal and silicate regoliths.

3 Methods

3.1 Sample Selection

Six equilibrated ordinary chondrite samples were sourced from the meteorite collection at the American Museum of Natural History (AMNH), two for each ordinary chondrite group (H, L, LL). The meteorite samples were chosen based on amounts of available material in the collection and ranged from petrologic types 4 to 6: Soko-Banja (LL4), Mangwendi (LL6), Mount Tazerzait (L5), Suizhou (L6), Jilin (H5), and Zhovtnevyi (H6). All samples were taken from the meteorite interior and are falls, meaning they experienced minimal terrestrial weathering.

3.2 Sample Characterization

3.2.1 Electron probe microanalysis (EPMA)

3.2.1.1 X-ray Element Mapping

Existing thin sections of Soko-Banja and Mangwendi and prepared polished thick sections of Mount Tazerzait, Suizhou, Jilin, and Zhovtnevyi were mapped in X-ray emission for elements Al, Ca, Cr, Fe, Mg, Na, Ni, S, Si, Ti (Jilin, Zhovtnevyi) and for elements Al, Ca, Cr, Fe, Mg, P, Ni, S, Si, Ti (Soko-Banja, Mangwendi, Mount Tazerzait, Suizhou) at 4 μm/pixel using a 1 μm beam, 40 nA beam current, 15 kV accelerating voltage, and 15 ms dwell time on the Cameca SX5 Tactis electron probe microanalyzer (EPMA) with five wavelength dispersive spectrometers (WDS) at the AMNH. Obtaining element maps over a sufficient area (~0.5 cm^2; Gemma and Ebel, 2019, 2021) enabled determination of relative modal mineral phase abundances, while also providing petrologic and compositional data to contextualize the samples chosen for spectroscopic analysis.

3.2.1.2 Determination of Modal Mineralogy

The resulting X-ray element maps were combined to create Red-Green-Blue (RGB) composite images using one element map in each color channel (e.g., Red = Mg, Green = Ca, Blue = Fe). The maps reveal visible textural differences with petrologic type. Figure 1 shows maps of sections of the LL chondrites Soko-Banja and Mangwendi. Soko-Banja, an LL chondrite with a petrologic type of 4, is considerably more pristine than its LL counterpart Mangwendi, of petrologic type 6. Inclusion boundaries of the spherical chondrules and individual mineral grains

are distinct in the map of the more pristine Soko-Banja, and not as obvious in the map of the more thermally altered Mangwendi.

These RGB maps provide a qualitative representation of mineralogy in the sample. To quantitatively address mineral diversity, acquired element maps were linearly combined to determine the mineralogy of each individual pixel in a map, following the methods of Crapster-Pregont and Ebel (2020). This enabled calculation of the relative modal mineral abundances across the mapped area in each meteorite. This method provides high resolution mineral abundances, as it can account for mineralogies at the micron scale while preserving petrographic context, unlike traditional methods such as point counting and destructive methods such as powder X-ray diffraction (XRD). The full modal mineral abundance maps for each meteorite analyzed in this study are included in the supplementary material (Figures S1 – S6). Calculated mineral abundances are reported in Table 1. Values are broadly consistent with those expected for meteorites from similar groups and petrologic types (Gastineau-Lyons et al., 2002; Dunn et al., 2010a).

	Soko-Banja (LL4)	**Mangwendi (LL6)**	**Mount Tazerzait (L5)**	**Suizhou (L6)**	**Jilin (H5)**	**Zhovtnevyi (H6)**
Olivine	43.54	45.07	40.26	43.3	35.32	35.12
Low-Ca Pyroxene	20.7	17.28	27.05	22.45	31.07	33.24
High-Ca Pyroxene	5.42	4.51	8.04	7.54	6.32	6.25
Mesostasis[#]	12.49	14.78	9.06	12.96	6.93	9.83
Kamacite	0.2	0.49	0.57	1.09	6.49	3.68
Taenite	0.54	0.88	1.51	1.34	0.92	0.97
Troilite	6.36	5.05	5.2	3.7	4.99	4.39
Ca-Phosphate	0.56	0.54	0.45	0.38	0.37	0.71
Chromite	0.41	0.56	0.57	0.46	0.7	0.44
Unknown	9.78	10.84	7.29	6.78	6.89	5.37
Metal*	0.74	1.37	2.08	2.43	7.41	4.65

Table 1. Calculated modal mineral abundances from polished thick and thin sections of the six meteorites evaluated in this study. The total abundance of Fe-Ni metal (*) is determined by combining the values for kamacite and taenite. The unknown component is predominantly attributable to pixels with a mix of mineral phases, either on grain boundaries or in the matrix component (where grain size << pixel size). [#]Mesostasis refers to chondrule glass recrystallized at the sub-micron scale, typically to plagioclase feldspar.

3.2.1.3 Quantitative Point Analysis

Quantitative analyses of the olivine and low-Ca pyroxene phases in ordinary chondrite chondrules were collected with the EPMA at AMNH to determine the iron contents of these two modally dominant mineral phases. Concentrations of elements Na, Mg, Al, Si, S, Ca, Ti, Mn, Fe, and Ni were determined using a 1 μm focused beam and a 20 nA beam current with an accelerating voltage of 15 kV. The average fayalite content (Fa) of the olivine analyses and ferrosilite content (Fs) of the low-Ca pyroxene analyses were then calculated for each meteorite and are reported in Table 2. Similar to the calculated mineral abundances, these compositions are broadly consistent with those determined for meteorites from similar groups and petrologic types (Rubin, 1990, 2005b; Weisberg et al., 2006).

3.2.2 Sample Powder Preparation

Samples were powdered by hand using an agate mortar and pestle and subsequently dry sieved into four separate size fractions: 25-63 μm, 63-90 μm, 90-125 μm, and 125-250 μm. This range of grain sizes is congruous with the reported grain sizes of returned regolith particles from asteroid Itokawa (30-180 μm; Tsuchiyama et al. 2011).

		Fa (mol%)			Fs (mol%)		
Meteorite	**Type**	**n**	**mean**	**σ**	**n**	**mean**	**σ**
Soko-Banja	LL4	64	27.98	0.6	53	21.25	1.6
Mangwendi	LL6	58	29.62	0.2	53	24.6	0.9
Mount Tazerzait	L5	75	25.02	0.2	73	20.94	1.06
Suizhou	L6	59	24.84	0.4	39	20.61	0.9
Jilin	H5	53	18.82	0.2	41	16.68	0.8
Zhovtnevyi	H6	53	19.28	0.3	30	17.08	0.6

Table 2. Olivine fayalite (Fa) contents and low-Ca pyroxene ferrosilite (Fs) contents of the six meteorites evaluated in this study. The number of analyses (n), mean, and 1 sigma (σ) values are reported for each meteorite.

3.2.3 X-Ray Diffraction

To assess whether the powdering and sieving process altered the relative mineral proportions in each size fraction, XRD measurements of the 24 sample powders (six meteorites at four different size fractions) were made on the Thermo Scientific ARL Equinox 100 X-Ray Diffractometer (XRD) at the AMNH at 45 kV and 0.3 mA following the methodology of Howard et al. (2009, 2011). Although the meteorite pieces used to produce powders for XRD differed from the slabs used for EMP mapping, the mineral abundances determined using the meteorite slabs are expected to be representative of the bulk meteorite and pieces derived from it (Gemma and Ebel, 2019, 2021). For the XRD measurements, approximately ~100 mg of each powdered sample was placed into an aluminum sample well and packed using the flat edge of a metal spatula to ensure a high degree of randomness in grain orientations and minimization of grain alignments. Each sample was analyzed for 20 minutes, and pure mineral standards of forsterite (Mg-endmember olivine), enstatite (Mg-endmember low-Ca pyroxene), and diopside (high-Ca pyroxene) powdered to the relevant size fraction (25-63 μm, 63-90 μm, 90-125 μm, or 125-250 μm) were analyzed after each sample to enable phase quantification. However, artifacts from grain size and grain size variability are a known complication for quantitative XRD (Cressey and Batchelder, 1998; Batchelder and Cressey, 1998; Bland et al., 2004; King et al., 2015a). Because the grain sizes of the samples in this study are much larger than the ideal grain size for quantitative XRD (<5 μm) and vary widely (up to 125 μm difference in grain size in the largest size fraction), the resulting XRD measurements are considered qualitative at best. The larger grains and variable grain sizes prohibited a completely smooth powder surface in the sample well, which likely resulted in microabsorption (beam attenuation due to surface roughness; Cressey and Batchelder, 1998; Bland et al., 2004).

The abundance ratios of olivine (olv) and low-Ca pyroxene (opx; short for orthopyroxene, which refers to the orthorhombic crystal structure of low-Ca (<5 mol %) pyroxenes) determined from the electron microprobe (EMP) for meteorite slabs and XRD for the smallest (25-63 μm) size fraction of each meteorite are compared in Figure 2a. XRD measurements generally produce higher olv/opx ratios than EPMA map analysis for all

meteorites except for Soko-Banja (LL4), the least altered meteorite in the measured suite, which plots just above the 1:1 line, and Mangwendi (LL6), which plots on the 1:1 line. The less altered H chondrite sample (Jilin) plots closer to the 1:1 line than its more altered counterpart (Zhovtnevyi). The high olv/opx ratio of the L5 meteorite Mount Tazerzait is anomalous, possibly because of differences in breakage during powdering due to its uniquely high porosity when compared to other L chondrites (Macke 2010; Friedrich et al., 2014). The general inconsistency between EPMA and XRD olv/opx ratios may be due to the non-ideal grain sizes of the samples used for XRD analysis, un-representative sub-sampling of the meteorite powder for XRD analysis, metal sinking to the bottom of the sample well, or inherent differences in ratio values due to the comparison of volume percent (XRD) and 2-dimensional mineral area (EPMA) abundances. However, Dunn et al. (2010a) found similar discrepancies in XRD- and EPMA-derived phase abundances of high-Ca pyroxene in ordinary chondrites and were able to attribute the differences to the exclusion of pigeonite in the EMP calculated diopside (high-Ca pyroxene) values.

The relative metal content in each size fraction of each meteorite is shown in Figure 2b. The metal content is represented by the diffraction intensity for the main diffraction peak of Fe-Ni metal in the XRD measurement for each size fraction. For meteorites in the same group, the 25-63 μm, 63-90 μm, and 90-125 μm size fractions have fairly uniform metal contents, which is to be expected for samples from the same group. However, it is obvious that the largest size fraction (125-250 μm) preferentially contains the metal for most meteorites. Metal coarsens as petrologic type increases, so the concentration of metal in the largest size fraction during powdering and sieving is not surprising. The comparatively low metal content of the largest size fraction of Mangwendi (LL6) may be due to less coarse metal grains (as observed in Figure 1d compared to Figure 1b) or a less uniform distribution of them in the meteorite, as it is the only brecciated sample in the suite.

3.3 VNIR Measurements

The Center for Planetary Exploration (CPEx) at Stony Brook University houses a custom planetary environmental spectroscopy chamber as part of the Vibrational Spectroscopy Laboratory (Glotch et al., 2016). The Planetary and Asteroid Regolith Spectroscopy Environment Chamber (PARSEC) is attached to a Thermo Nicolet iS50 Fourier Transform Infrared spectrometer, enabling emissivity measurements, as well as an Analytical Spectral Devices (ASD) FieldSpec3 Max UV-VIS-NIR spectrometer coupled to the chamber with a 1° field of view (FOV) foreoptic, allowing for laboratory bidirectional reflectance measurements over 0.35-2.5 μm. PARSEC is able to sustain a vacuum of $< 10^{-5}$ mbar while accommodating a six-sample rotating stage with heated aluminum sample cups and a liquid nitrogen cooled radiation shield. An attached solar illumination lamp along with internal optics permits measurements of MIR (2000-400 cm^{-1}) emissivity and VNIR (0.35-2.5 μm) reflectance spectra in a simulated lunar or asteroid environment.

Using PARSEC and the attached ASD UV-VIS-NIR spectrometer, VNIR reflectance spectra of the 24 ordinary chondrite samples were collected, at incidence and emission angles i = 55° and e = 41°. Following the methods of Hinrichs and Lucey (2002), a borosilicate glass window was placed in front of the solar lamp, cutting off light greater than ~2.5 μm. As such, the sample temperatures were controlled solely by heating of the sample cups from below, which induced a thermal gradient in the sample that simulates the surface regolith thermal environment on airless bodies. The average chamber pressure of PARSEC for these measurements was

438 ~1.2x10^{-5} mbar, and the chamber environment was kept at a constant temperature of -140 °C,
439 again to mimic the surface environment of airless bodies (Shirley and Glotch, 2019). These
440 conditions – low intensity illumination, ~10^{-5} mbar chamber pressure, and -140 °C chamber
441 temperature – are used to define simulated asteroid surface conditions for this work. A
442 Spectralon reflectance standard placed inside the chamber was measured prior to each sample
443 measurement. For the dark current, reference, and sample spectra, 5000 scans were taken and
444 averaged together. For each size fraction of each ordinary chondrite sample, the averaged
445 reflectance spectrum was recorded at a series of temperatures relevant to NEAs, in increments of
446 10 degrees from 10 °C to 100 °C, for a total of ten spectra per size fraction of each meteorite.
447 This chosen temperature range covers both the surface temperature of the Hayabusa touchdown
448 site (36.85 ± 10 °C) and the global averaged daytime temperature (66.85 ± 10 °C) of the
449 Hayabusa target and ostensible ordinary chondrite parent body, asteroid 25143 Itokawa (Okada
450 et al., 2006).
451 Comparison of successive measurements of the same sample confirm that the 5000 scan
452 average enables precise replication of measurements with negligible instrumental error. Three
453 VNIR measurements of the 25-63 μm size fraction of Suizhou (L6) taken at 10 °C over three
454 consecutive days are plotted in supplementary Figure S7 along with their standard deviation. The
455 average standard deviation across the entire target wavelength range (0.55-2.5 μm) is 0.0005,
456 and the average standard deviations for Band I and Band II are 0.0005 and 0.0002 respectively.
457
458 *3.4 Spectral Processing*
459 The resulting 240 VNIR reflectance spectra were splice corrected using ASD's RS^3
460 spectral acquisition software and exported for further analysis. Davinci, spectroscopic analysis
461 software developed at Arizona State University, was used to perform continuum removals on the
462 spectra, enabling quantitative comparison of band parameters among the spectra. The continuum
463 is removed via an algorithm in Davinci following the mathematics outlined in Clark and Roush
464 (1984). The continuum was removed separately for Band I and Band II. Wavelength positions of
465 continuum removal endpoints are reported in supplementary Table S1.

Table 3

	Size Fraction (µm)	Band I Center (µm)	Band I Minimum	Band I FWHM (µm)	Band I Asymmetry	Band II Center (µm)	Band II Minimum	Band II FWHM (µm)	Band II Asymmetry	Band Area Ratio (Band II/Band I)
Soko-Banja (LL4)	25-63	0.976	0.78469	0.4009	0.55413	1.961	0.94666	0.41128	1.29325	0.23128
	63-90	0.962	0.64493	0.40509	0.51018	1.945	0.87977	0.42629	1.11832	0.32815
	90-125	0.962	0.64648	0.42316	0.50071	1.939	0.87776	0.40378	1.11856	0.31311
	125-250	0.954	0.63466	0.37375	0.51907	1.94	0.84062	0.43056	1.16392	0.44727
Mangwendi (LL6)	25-63	0.978	0.72473	0.41459	0.55697	1.962	0.94115	0.41269	1.06537	0.19009
	63-90	0.974	0.59078	0.44713	0.53424	1.947	0.89517	0.40339	1.11861	0.22621
	90-125	0.97	0.60596	0.43766	0.54092	1.943	0.87908	0.41565	1.12482	0.28708
	125-250	0.978	0.6083	0.45898	0.55454	1.948	0.88596	0.40889	1.21329	0.24928
Mount Tazerzait (L5)	25-63	0.937	0.61164	0.34373	0.4583	1.936	0.86511	0.44873	1.15946	0.38089
	63-90	0.943	0.49048	0.39083	0.46551	1.932	0.79184	0.45839	1.20955	0.41974
	90-125	0.947	0.50514	0.40992	0.4797	1.944	0.78904	0.46432	1.16072	0.4579
	125-250	0.954	0.47978	0.44079	0.49028	1.952	0.78591	0.45404	1.18357	0.42052
Suizhou (L6)	25-63	0.939	0.66047	0.35991	0.43899	1.952	0.88913	0.44541	1.20239	0.35782
	63-90	0.935	0.53826	0.33417	0.49866	1.935	0.80547	0.45521	1.18397	0.50049
	90-125	0.939	0.5414	0.33789	0.50009	1.936	0.8108	0.46003	1.18294	0.49046
	125-250	0.937	0.5379	0.32415	0.5252	1.936	0.79323	0.46887	1.15811	0.55679
Jilin (H5)	25-63	0.922	0.82218	0.24701	0.50337	1.972	0.94656	0.43076	1.42671	0.38722
	63-90	0.923	0.69421	0.26608	0.49752	1.937	0.87515	0.4349	1.13236	0.55377
	90-125	0.926	0.69508	0.27774	0.65012	1.925	0.85857	0.43968	1.14282	0.63841
	125-250	0.926	0.71832	0.27206	0.82278	1.923	0.87354	0.43721	1.16529	0.62565
Zhovtnevyi (H6)	25-63	0.926	0.72997	0.28872	0.46199	1.918	0.89828	0.43093	1.1972	0.50073
	63-90	0.928	0.59507	0.30198	0.47714	1.918	0.80751	0.44381	1.19625	0.61628
	90-125	0.933	0.61107	0.3139	0.48143	1.919	0.82503	0.45035	1.67006	0.56361
	125-250	0.933	0.62517	0.30708	0.49956	1.92	0.82924	0.44948	1.20793	0.58022

Table 3. Calculated band parameters for the 10 °C measurements of all size fractions of all meteorites.

Spectra were then fit using the Modified Gaussian Model (MGM) as defined in equation 4 of Sunshine et al. (1990):

$$m(x) = s * exp\left\{\frac{-(x^n-\mu^n)^2}{2\sigma^2}\right\} \quad (1)$$

where the modified Gaussian distribution in a random variable *x*, *m(x)* is expressed in terms of its center μ (mean), width σ (standard deviation), strength *s* (amplitude), and exponent *n* (Sunshine et al., 1990). For mafic multi-mineralic VNIR spectra, the MGM is preferred because it accounts for asymmetry in absorption bands caused by the multiple absorptions near 1 μm and 2 μm for olivine and pyroxene mixtures, unlike the purely symmetric Gaussian model fit (Sunshine and Pieters, 1993; Figure S8). Altering the value of the exponent *n* adjusts the symmetry of the distribution to better fit the slopes of the right and left wings of the band (Sunshine et al., 1990). In this work, *n = -1* was used for model fits of Band I, consistent with the Band I analyses in Sunshine et al. (1990) and Sunshine and Pieters (1993). For model fits of Band II, *n = 2* was used.

Common spectral parameters (band center, band minimum, and full width at half maximum (FWHM)) for both Band I and Band II were calculated using the model fits. The band area ratio (BAR; Band II area/Band I area) and band asymmetry ratio (band area to the left of the band center divided by the band area to the right of the band center) were calculated using the trapezoidal rule to enable direct comparison with band area values of ordinary chondrites and NEAs from Dunn et al. (2010c, 2013). Band parameter values for the 10 °C measurements of all size fractions of all meteorites are reported in Table 3. Band parameter values for all other temperature measurements of each size fraction of each meteorite are reported in supplementary Tables S2 through S7.

4 Results

Here we evaluate the conditions that contribute to variations in the VNIR spectral data set: sample composition (both metal content and silicate composition), sample particle size, and measurement temperature. The effects of these parameters on the spectra will first be evaluated individually and then collectively in the following sections.

4.1 VNIR Spectral Data

The 10 °C VNIR spectra of the 25-63 μm size fraction of all meteorites are shown in Figure 3. These data are representative of the general differences in spectral character due to the varying composition of the samples (as detailed in Tables 1 and 2). The spectra are arbitrarily offset on the y-axis for clarity, and meteorites from the same ordinary chondrite group are paired together. The characteristic absorptions near 1 μm (due to the presence of olivine and pyroxene) and 2 μm (due to the presence of pyroxene) are evident, as is a weak absorption near 1.3 μm. Gaffey (1976) attributed this feature to the presence of anorthite feldspar (Gaffey, 1976, his Fig. 18), which is the third most modally abundant phase in ordinary chondrites after olivine and low-Ca pyroxene, produced due to the metamorphic re-crystallization of chondrule mesostasis. Johnson and Hörz (2003) and Cheek et al. (2009) attribute changes in the strength of the broad absorption band of anorthosite at ~1.3 μm to Fe^{2+} in feldspars. Examining the spectra of the H and LL meteorites in Figure 3, the two most compositionally different of the ordinary chondrite groups, the 1 μm feature is noticeably broader and more absorptive in the LL spectra, due to the higher Fa content of the LL olivine.

Albedo effects due to sample particle size are evident in Figure 4a, which shows the unprocessed 10 °C VNIR spectra of all size fractions of the H5 chondrite Jilin. Albedo clearly

decreases as the particle size increases, with the smallest size fraction (25-63 μm) having a significantly higher albedo than the three larger size fractions (63-90 μm, 90-125 μm, and 125-250 μm). Slight changes in spectral shape due to particle size are also perceptible – the spectrum of the smallest size fraction displays absorption features that are narrower and sharper than those observable in the largest size fraction. Additionally, the 1.3 μm feature disappears almost entirely in the spectrum of the largest size fraction of Jilin in Figure 4a. Spectral variation due to temperature is observable in Figure 4b, which plots the unprocessed VNIR spectra for all ten temperature measurements (10 °C – 100 °C) of the 25-63 μm size fraction of Jilin. A small but noticeable shifting of the spectral shape due to changes in temperature is apparent near the 1.5 μm reflectance maximum that continues down the shorter wavelength shoulder of the 2 μm absorption feature, though the temperature spectra plot essentially on top of each other at longer and shorter wavelengths.

4.2 Spectral Variation due to Temperature

To more quantitatively evaluate spectral changes, band parameters were calculated as described in Section 3.4. The temperature data set consists of the full 240 VNIR spectra – ten temperature measurements (10 ºC - 100 ºC) for each of the four size fractions of the six measured meteorites. Calculated band parameters for all 240 VNIR spectra are plotted in supplementary Figures S9 – S17. The differences in band parameter values for the 10 °C and 100 °C temperature measurements are explored in the following sections. All changes in spectral features discussed in this section are due to temperature unless otherwise noted.

4.2.1 Band I

The differences due to temperature in calculated Band I parameters are shown in Figure 5. Here, the percent difference has been calculated between the lowest (10 ºC) and highest (100 ºC) temperature measurement to summarize the spectral changes across the full measured temperature regime. Positive percent difference values indicate that the band parameter value increased as temperature increased from 10 ºC to 100 ºC. Negative percent difference values indicate that the band parameter value decreased as temperature increased. All differences in Band I parameter values due to temperature changes are less than ±5%. The Band I centers (Figure 5c,g,k,o) change the least; all calculated percent difference values plot essentially at zero. The Band I minima (Figure 5b,f,j,n) also demonstrate minimal changes, although the slight changes in the Band I minima values for three largest size fractions (63-90 μm, 90-125 μm, 125-250 μm) suggest some dependency on composition, as the degree of band minima change varies with group type. The Band I FWHM (Figure 5a,e,i,m) and Band I asymmetry values (Figure 5d,h,l,p) vary more strongly and less uniformly across meteorites and size fractions due to changes in temperature.

The Band I FWHM for the 25-63 μm size fraction (Figure 5a) decreases with temperature for the LL chondrites and increases with temperature for the L chondrites, but increases for the less altered H chondrite and decreases with temperature for the more altered H chondrite. The Band I FWHM for the 63-90 μm size fraction (Figure 5e) also increases for the H5 chondrite and decreases with temperature for the H6 chondrite, but does the opposite for the L5 and L6 chondrites, while showing no change for the LL6 chondrite and decreasing by over 4% for the LL4 chondrite. The Band I FWHM for the 90-125 μm size fraction (Figure 5i) remains essentially at zero for the LL4, LL6, and L6 chondrite, but decreases by nearly 2% for the L5, H5, and L6 chondrites. The Band I FWHM for the 125-250 μm size fraction (Figure 5m)

increases by 1-2% for the H chondrites, but decreases for the less altered LL and L chondrites and increases with temperature for the more altered LL and L chondrites.

The Band I asymmetry difference due to temperature for the 25-63 μm size fraction (Figure 5d) decreases for the samples of lower petrologic type in each group, is essentially zero for the LL6 and L6 chondrites, and increases for the H6 chondrite. For the 63-90 μm size fraction (Figure 5h), the difference in Band I asymmetry is very close to zero for the LL6, L5, and L6 chondrites, is negative (decreases) for the LL4 and H5 chondrites, and is positive (increases) for the H6 chondrite. For the 90-125 μm size fraction (Figure 5l), the Band I asymmetry increases for the L5 and H5 chondrites, and decreases for all other samples, though the differences for both the L5 and L6 chondrites remain close to zero. For the 125-250 μm size fraction (Figure 5p), the Band I asymmetry decreases for all samples except the L5 chondrite. The H5 chondrite Jilin has a particularly strong decrease (~5%) due to the change in temperature from 10°C to 100°C in the 125-250 μm size fraction.

4.2.2 Band II

The differences due to temperature in calculated Band II parameters are shown in Figure 6. As in Figure 5, the percent difference has been calculated between the lowest temperature measurement (10ºC) and highest (100ºC) temperature measurement to summarize the spectral changes across the full measured temperature regime. All differences in Band II parameter values due to temperature changes are also less than ±5%.

The Band II centers (Figure 6c,g,k,o) change the least; all calculated percent difference values plot essentially at zero, with the exception of the smallest size fraction. The Band II minima (Figure 6b,f,j,n) also demonstrate minimal changes, although the majority of the Band I minima values for three largest size fractions (63-90 μm, 90-125 μm, 125-250 μm) slightly increase due to changes in temperature. The Band II FWHM (Figure 6a,e,i,m) and Band II asymmetry values (Figure 6d,h,l,p) vary much more strongly and less uniformly across meteorites and size fractions due to changes in temperature, as seen for Band I.

The Band II FWHM for the 25-63 μm size fraction (Figure 6a) increases with temperature for all samples except for the LL6 chondrite, which plots at zero. The 25-63 μm size fraction of the H5 chondrite Jilin has a particularly large increase (>4%) in the Band II FWHM. The Band II FWHM for the 63-90 μm size fraction (Figure 6e) does not seem to change with temperature for the LL and L chondrites, but decreases with temperature for the H5 chondrite and increases for the H6 chondrite. The Band II FWHM for the 90-125 μm size fraction (Figure 6i) increases for the LL4, L6, and H6 chondrites, decreases more strongly for the LL6 chondrite, and does not change for the L5 and H5 samples. The Band II FWHM for the 125-250 μm size fraction (Figure 6m) decreases by 1-2% for the LL chondrites, but increases only slightly with temperature for the L and H chondrite groups.

The Band II asymmetry difference due to temperature for the 25-63 μm size fraction (Figure 6d) decreases for the samples of lower petrologic type in the LL and H groups, and the L6 chondrite, does not change for the L5 chondrite, and increases for the samples of higher petrologic type in the LL and H groups. For the 63-90 μm size fraction (Figure 6h), the difference in Band II asymmetry more strongly increases for the LL chondrites and H5 chondrite, and decreases slightly for the L5, L6, and H6 samples. For the 90-125 μm size fraction (Figure 6l), the Band II asymmetry strongly increases for the LL4 chondrite (>4%), slightly increases for the L6 chondrite, and decreases for the remaining chondrites. For the 125-

250 μm size fraction (Figure 6p), the Band II asymmetry slightly decreases for all samples except the LL6 chondrite, which more strongly decreases.

4.2.3 Band Area Ratio

The differences due to temperature for the calculated band area ratios (BARs; Band II area/Band I area) of all size fractions of all meteorites are displayed in Figure 7. There is no uniform change in BAR across size fractions or ordinary chondrite groups, but the percent differences are generally larger in value than those examined in Figures 5 and 6. The BARs all slightly increase due to the 10-100°C temperature change for the 25-63 μm size fraction (Figure 7a), with the exception of the H5 chondrite Jilin, whose BAR strongly (~20%) increases due to the temperature change. For the 63-90 μm size fraction (Figure 7b), the BARs all decrease, with the L6 and H6 samples decreasing slightly less than their L5 and H5 counterparts, while the LL6 sample decreases slightly more than its LL4 counterpart. For the 90-125 μm size fraction (Figure 7c), the same trend of the L6 and H6 samples decreasing slightly less than their L5 and H5 counterparts is apparent. However, in Figure 7c, the LL4 sample slightly increases due to the change in temperature, while the LL6 sample more strongly decreases (~7%) due to the change in temperature. For the 125-250 μm size fraction (Figure 7d), the LL6 and L6 samples decrease slightly more with temperature than their LL4 and L5 counterparts, while the H5 sample strongly decreases (~7%) and the H6 sample increases (~5%) due to changes in temperature.

4.3 Spectral Variation due to Particle Size

The 10°C temperature measurements for all size fractions of all meteorites were used to evaluate changes in band parameter values due to differences in particle sizes. This subset of 24 VNIR spectra is explored in the following sections. All changes in spectral features discussed in this section are due to particle size unless otherwise noted.

4.3.1 Band I

The variations in Band I parameter values due to particle size are shown in Figure 8. The Band I FWHM values are displayed in Figures 8a-c for the LL, L, and H chondrites, respectively. The FWHM values of samples of higher petrologic type in the LL and H groups (Mangwendi and Zhovtnevyi) are greater than those for the samples of lower petrologic type (Soko-Banja and Jilin) in the same group. This trend is mostly reversed for the L chondrites (Figure 8b) where the largest three size fractions of the L5 chondrite Mount Tazerzait have Band I FWHM values that are larger than those for the L6 chondrite Suizhou. Additionally, the FWHM value increases as particle size increases for Mount Tazerzait, but decreases as particle size increases for Suizhou. For the H chondrites (Figure 8c), the Band I FWHM value increases as particle size increases for the smallest three size fractions, but then slightly decreases for the largest size fraction. While there seems to be an overall trend of FWHM value increasing as particle size increases for the LL chondrites (Figure 8a), the trend is not uniform and the FWHM value for the largest size fraction of Soko-Banja is actually less than that of the three smaller size fractions.

Figures 8d-f show the Band I minima values for all size fractions of the six meteorites. Again, the LL and H chondrites (Figures 8d,f) show a clear and consistent trend, with the more thermally altered sample in the group having a lower Band I minimum than its less altered group partner. The smallest size fraction for both meteorites in both groups has the highest Band I minimum, or highest reflectance, while the three larger size fractions for both meteorites in both groups have lower Band I minima that are similar in value. Notably, the largest size fraction of the H chondrite samples has a slightly higher Band I minimum than the 63-90 μm and 90-125

μm size fractions. The L chondrites (Figure 8e) display the opposite trend - the less thermally altered sample in the group, Mount Tazerzait, has lower Band I minima for all size fractions than those for its more altered pair, Suizhou. However, the smallest size fraction of both L chondrites has the highest reflectance out of all the size fractions, and the larger size fractions are more absorptive and have similar values, consistent with that seen for the LL and H chondrites.

Variations in the Band I center due to particle size are displayed in Figures 8g-i for all size fractions of the six meteorites. Again, opposite trends are observed for the L chondrites when compared to the LL and H chondrites. The Band I centers for the LL6 and H6 chondrites are at longer wavelengths than those for their less thermally altered pair (LL4 and H5, respectively), whereas the L6 chondrite Suizhou has Band I centers at shorter wavelengths for the three largest size fractions than its less altered pair, Mount Tazerzait (L5). The smallest size fraction of Suizhou does have a Band I center value at longer wavelengths than that of Mount Tazerzait, however. There also appears to be an increase in the Band I center position as particle size increases for the L5, H5, and H6 chondrites. In contrast, the LL4 chondrite shows a decrease in the Band I center position as particle size increases, as does the LL6 chondrite, with the exception of the largest size fraction. The Band I center of the L6 chondrite Suizhou stays relatively the same as particle size increases.

Variations in the Band I asymmetry due to particle size for all size fractions of the six meteorites, shown in Figures 8j-l, display less consistent trends than other Band I parameters. The LL chondrites (Figure 8j) have similar and relatively consistent Band I asymmetry values, with the less thermally altered sample having slightly smaller Band I asymmetry values than the more altered sample. For the L chondrites (Figure 8k), the Band I asymmetry values for both samples increase as particle size increases. For the three largest size fractions of the L chondrites, the L6 chondrite has a larger Band I asymmetry value than the L5 chondrite, with the smallest size fraction of the L6 chondrite having just a slightly smaller value than the L5 chondrite. The H chondrites (Figure 8l) show different trends – Band I asymmetry values for the H6 chondrite increase slightly as particle size increases, whereas the values for the H5 chondrite are relatively similar for the smallest two size fractions, but significantly higher for the largest two size fractions. Also, unlike the majority of the LL and L samples, the Band I asymmetry values for the H chondrite of lower petrologic type are greater than the H chondrite of higher petrologic type.

4.3.2 Band II

The variations in Band II parameter values due to particle size are shown in Figure 9. The Band II FWHM values are displayed in Figures 9a-c for the LL, L, and H chondrites, respectively. The Band II FWHM values tend to increase as particle size increases for the L and H chondrite samples (Figure 9b and c respectively), with the exception of the largest size fraction of the L5 chondrite Mount Tazerzait, which has a Band II FWHM value less than that of the next two smallest size fractions. The H6 chondrite (Figure 9c) has slightly larger Band II FWHM values than the H5 chondrite, whereas the L5 and L6 chondrites have very similar values, again with the exception of the largest size fraction (Figure 9b). The Band II FWHM values have an abnormal pattern as particle size increases for the LL chondrites (Figure 9a). The Band II FWHM values for the LL4 chondrite increase from the smallest to the next smallest size fraction, then decrease, then increase again for the largest size fraction. The Band II FWHM values for the LL6 chondrite follow the exact opposite pattern – decreasing from the smallest to next smallest size fraction, then increasing, then decreasing again for the largest size fraction.

Figures 9d-f show the Band II minima values for all size fractions of the six meteorites. The H chondrites (Figure 9f) show the same pattern for the Band II minima values as for the Band I minima values - the smallest size fraction for both meteorites has the highest Band II minimum, or highest reflectance, with the next two size fractions having lower Band II minima values, and the largest size fraction then having a slightly higher Band II minima value. This trend also holds for the LL6 size fractions (Figure 9d), but does not hold for the LL4 size fractions, though there is an overall decrease in Band II minima values as particle size increases for the LL4 sample. The LL4 chondrite Band II minima values are also not consistently higher than those for the LL6 chondrite, as was observed in Band I. The L chondrites (Figure 9e), however, do show the same trend as observed in Band I, where the less thermally altered sample, Mount Tazerzait, has lower Band II minima for all size fractions than those for its more altered pair, Suizhou. The smallest size fraction of both the LL and L chondrites has the highest reflectance out of all the size fractions.

Variations in the Band II center due to particle size are displayed in Figures 9g-i for all size fractions of the six meteorites. The Band II center position decreases from the smallest to the second largest size fraction, then increases slightly for the largest size fraction for both LL chondrites (Figure 9g). The LL6 chondrite has Band II centers at slightly longer wavelengths than the LL4 chondrite for all size fractions. For the L chondrites (Figure 9h), the Band II center position shifts to shorter wavelengths as particle size increases for the L6 chondrite, and moves to longer wavelengths as particle size increases for the L5 chondrite. For the H chondrites (Figure 9i), the Band II center position strongly decreases as particle size increases for the H5 chondrite, but slightly increases as particle size increases for the H6 chondrite.

Finally, variations in the Band II asymmetry values due to particle size are shown in Figures 9j-l for all size fractions of the six meteorites. The Band II asymmetry values increase as particle size increases for the LL6 chondrite (Figure 9j), but then decrease and plateau for the LL4 chondrite. For the L chondrites (Figure 9k), the Band II asymmetry values stay relatively similar as particle size increases, but there is a slight decrease in the Band II asymmetry values for the L6 chondrite Suizhou. The H chondrites show much more variation in the Band II asymmetry values (Figure 9l). The Band II asymmetry values for the H5 chondrite Jilin generally decrease as particle size increases, but the largest size fraction has a slightly larger Band II asymmetry value than the second largest size fraction. The Band II asymmetry value for the 90-125 μm size fraction of Zhovtnevyi is much higher than any other values for the H chondrites. For all size fractions except the smallest, Zhovtnevyi (H6) has a higher Band II asymmetry value than Jilin (H5).

The LL and H chondrites share a trend involving the largest and smallest size fractions. For the smallest size fraction, the meteorite of lower petrologic type has a higher Band II asymmetry than the meteorite of higher petrologic type. For the largest size fraction, the meteorite of lower petrologic type has a lower Band II asymmetry than the meteorite of higher petrologic type. As seen for other band parameters, the opposite trend exists for the L chondrites – for the smallest size fraction, the meteorite of lower petrologic type has a lower Band II asymmetry than the meteorite of higher petrologic type, and for the largest size fraction, the meteorite of lower petrologic type has a higher Band II asymmetry than the meteorite of higher petrologic type.

4.3.2 Band Area Ratio

742 The variations in BAR values due to particle size are shown in Figure 10. There is no
743 uniform change across particle size or ordinary chondrite group for the BAR values. For the LL
744 chondrites (Figure 10a), the meteorite of lower petrologic type has larger BAR values than the
745 meteorite of higher petrologic type. The BAR also broadly increases as particle size increases for
746 the LL chondrites, with the exception of the largest size fraction of the LL6 chondrite, whose
747 BAR value decreases slightly compared to the second largest size fraction. The L chondrites in
748 Figure 10b again show an opposite trend – the meteorite of higher petrologic type has larger
749 BAR values than the meteorite of lower petrologic type for all size fractions except the smallest,
750 where the BAR values for the two L chondrites are very similar. The BAR of the L chondrites
751 also broadly increases as particle size increases, but with the exception of the largest size fraction
752 of the L5 chondrite, whose BAR value decreases slightly compared to the second largest size
753 fraction. The H chondrites (Figure 10c) show a mix of trends. The BAR increases for both
754 meteorites as particle size increases, but the BAR for the H6 chondrite is higher than that of the
755 H5 chondrite for the smallest two size fractions, then smaller than that of the H5 chondrite for
756 the largest two size fractions.
757
758 *4.3.3 Spectral Slope*
759 Spectral slopes calculated for the 10°C temperature measurement of all size fractions of
760 all meteorites are shown in Figure 11. There is a clear correlation in spectral slope values and
761 particle size – for each meteorite, the spectral slope value gets progressively more negative as the
762 particle size increases. This is reflected in the high R^2 values for each meteorite, all of which are
763 >0.85, indicating significance in the relationship between spectral slope value and particle size.
764 The LL chondrites (Figure 11a) display the largest changes in spectral slope due to
765 particle size, with the smallest size fractions displaying spectral slopes near zero and the largest
766 size fractions displaying spectral slopes between -0.024 and -0.031. The H chondrites (Figure
767 11c) have a comparatively smaller change in spectral slope due to particle size, as the smallest
768 size fractions have spectral slopes that are already quite negative, between -0.011 and -0.016,
769 while the largest size fractions have spectral slopes between -0.026 and -0.031. However, both
770 the LL and H chondrites demonstrate a trend with petrologic type – the 25-63 μm size fraction of
771 the less altered LL sample has a less negative spectral slope than the more altered LL sample, but
772 that trend reverses as particle size increases, with the largest size fraction of the less altered LL
773 sample having a more negative spectral slope than the largest size fraction of the more altered LL
774 sample. The H chondrites show the opposite trend – the 25-63 μm size fraction of the less
775 thermally altered H sample has a more negative spectral slope than the more altered H sample,
776 but that trend reverses as particle size increases, with the largest size fraction of the less
777 thermally altered H sample having a less negative spectral slope than the largest size fraction of
778 the more altered H sample. As for the L chondrites (Figure 11b), the spectral slope is the same
779 for the smallest size fraction of the L chondrite samples. As particle size increases, the spectral
780 slopes of both L chondrite samples become more negative, but the more thermally altered L
781 chondrite sample has consistently more negative spectral slopes for the three largest size
782 fractions than the less altered chondrite sample.
783
784 **5 Discussion**
785 *5.1 Spectral Contributions of Temperature and Particle Size*

Untangling the contributions of temperature, particle size, and composition on the spectral variations observed in this suite of ordinary chondrite meteorites is predictably complex, as more than one of these parameters can influence the observed changes in spectral features.

For example, VNIR spectral slope values of mafic silicates can be affected by both particle size (Reddy et al., 2015) and metal content (Gaffey 1976). Increased particle size is understood to make spectral slopes more negative (bluer; Reddy et al., 2015), whereas increased metal is understood to dampen spectral features of silicates and make the spectral slopes more positive (redder; Gaffey 1976). As seen in Figure 11, the spectral slopes of the meteorite samples examined in this study become more negative as particle size increases. Interestingly, the samples with the highest metal content, the H chondrites (Figure 11c) have the most negative spectral slopes to begin with, which only get more negative as particle size increases. Given their higher metal content, one would expect the H chondrites to display more positive (redder) slopes than the samples with the least amount of metal (the LL chondrites). The degree to which particle size and metal content are individually contributing to the spectral slope values is unclear. Future work examining the spectral features of the same silicate-metal mixture of different size fractions with and without the metal fraction could more quantitatively constrain the relative contributions of particle size and metal to spectral slope values.

The effects of temperatures in the NEA temperature regime (10-100ºC) on the VNIR spectra of the meteorites measured in this study are largely minimal. Temperature affects the FWHM and band asymmetry values for Band I and Band II most strongly, but the degree of differences is small (Figures 5, 6, S8-S16). The percent differences in VNIR band parameters between the coolest (10°C) and hottest (100°C) temperature measurements are all less than ±5% for Band I and Band II (Figures 5, 6). The band minimum and band center parameters are the least sensitive to temperature differences for the six meteorites examined, with their values remaining essentially constant as temperature increases.

For the band parameters that do appear to vary with temperature (FWHM and band asymmetry), trends with temperature are not consistent across all ordinary chondrite groups or across all size fractions. The band parameter values increase with temperature for some meteorites and some particle sizes, and decrease for others (e.g., Figure 5a,d,m).

For Band I and to a lesser extent Band II, the band asymmetry and FWHM for the H5 chondrite Jilin are most sensitive to temperature (Figures 5, 6). This chondrite sample has the largest difference values for nearly every size fraction for these two band parameters. Perhaps not coincidentally, it also has the largest metal content (Table 1). It is therefore possible that spectral effects due to temperature are stronger for silicate and metal mixtures with higher metal contents. This is a particularly important consideration for interpretation of the multispectral imager data from the NASA Psyche mission target, asteroid 16 Psyche, thought to have a silicate regolith with high metal content (Takir et al., 2017; Elkins-Tanton et al., 2020; Shepard et al., 2021).

Similar to the FWHM and band asymmetry, BAR is sensitive to temperature (Figure 7), but changes in BAR values as temperature increases are not consistent across ordinary chondrite groups or petrologic types within each group. The majority of BAR for the 63-90 μm, 90-125 μm, and 125-250 μm size fractions (Figure 7b,c,d) decrease up to ~10% with temperature, while the BAR of the 90-125 μm LL4 sample and the 125-250 μm H6 sample actually increase up to ~5% due to the change in temperature. In contrast, the BAR values of the 25-63 μm size fractions of all meteorites increase as temperature increases. Here we see the combined effects of temperature and particle size – for the smallest measured particle sizes, increasing temperature

causes the BAR to increase, not decrease as it does for larger particle sizes across the same temperature range. Exploring spectral effects for an extended temperature and particle size range would facilitate deconvolution of the combined effects of temperature and particle size on the BAR.

Once more, the H5 chondrite Jilin shows the strongest change in BAR values due to temperature, in particular for the 25-63 μm (Figure 7a; ~+20%) and 125-250 μm (Figure 7d; ~-7%) size fractions. The primary property distinguishing it from the other meteorites in this study is its metal content (Table 1, Figure 2), which would imply that this is a strong contributing factor. However, this would be in disagreement with the conclusion of Hinrichs and Lucey (2002) that neutral metal in ordinary chondrites does not contribute a temperature varying signal to the VNIR spectra.

Previous workers (Roush and Singer, 1986; Moroz et al., 2000; Hinrichs and Lucey, 2002; Sanchez et al., 2012) have observed temperature-induced spectral effects on all band parameters (band centers, band minima, FWHM, band asymmetry, and BAR) in mineral and meteorite spectra, and developed corrections to account for these observations. However, these changes were observed over a much greater temperature range, typically 80K - 400 K (-193.15°C to 126.85°C). In the NEA temperature regime that is investigated here (10°C - 100°C), spectral effects are effectively negligible for the band center and band minimum parameters, and minimal (<4%) for band asymmetry and band FWHM.

The magnitudes of particle size effects on spectral features of the ordinary chondrites examined in this study are much greater than those of temperature (Figures 8, 9, 10). The full range of particle sizes investigated (25-250 μm) encompasses the reported grain sizes of 30-180 μm returned particles from the NEA Itokawa (Tsuchiyama et al., 2011). Though some authors have noted that band parameters such as band center, band width, and band area for mineral mixtures are generally unaffected by particle size (Cloutis et al., 1986; Sunshine et al., 1993), others have identified particle size as an important factor when considering spectral variations in multi-mineralic samples (Cooper and Mustard, 1999; Cloutis et al., 2013). We find that particle size distinctly affects all examined band parameters for ordinary chondrite meteorite powders. This makes particle size an important factor to consider in the interpretation of asteroid spectra, as it has the potential to produce incorrect interpretations of asteroid regolith mineralogy that are derived from band parameter values.

Band parameter values change fairly consistently as particle size increases, but the trends do vary among the ordinary chondrite groups. For example, the Band I minima values initially decrease as particle size increases, but then increase for the largest size fraction of the LL and H chondrites (Figure 8). The Band I minima are also consistently higher for the samples of lower petrologic type in the LL and H groups than for the samples of higher petrologic type. In other words, the more thermally altered sample is more absorptive than the less altered sample for these two chondrite groups. In contrast, the Band I minima values for the largest size fraction of the L group are smaller than those of the smaller size fractions of the L chondrites. Additionally, the Band I and Band II minima are consistently higher for the L chondrite of higher petrologic type, meaning the more altered sample is more reflective than the less altered sample for the L chondrites, which is the opposite of what was seen for the LL and H band minima. Regardless of the ordinary chondrite group, there is a systematic variation in band minima due to particle size and petrologic type. Cloutis et al. (1986) claimed that the Band I center does not deviate due to particle size, but systematically deviates if mineral phases have significantly different Fe content or there is “more than a few percent of clinopyroxene”. The current work shows that the Band I

center does deviate with particle size as well as with Fe content, which typically increases slightly as petrologic type increases.

Band center values are used to characterize Fe content in spectroscopically observed olivine and pyroxene mixtures, and also for ordinary chondrites (Dunn et al., 2010c and references therein). To enable direct comparison between the ordinary chondrite spectra analyzed in this work and in Dunn et al., (2010c), we have recalculated band parameters for the spectra in Dunn et al., (2010c) using the MGM method, instead of using the reported band parameters determined using polynomial fitting. Equation 6 from Dunn et al., (2010c) describes the relationship between Fa content and the Band I center. Rederiving this equation for the Dunn et al., (2010c) band parameters calculated using the MGM method yields:

$$Fa = -1602.35 \times (BIC)^2 + 3127.216 \times (BIC) - 1584.17 \quad (2)$$

However, Figures 8 and 9 show that there are distinct differences in band centers due to particle size for the same meteorite. The Band I center differences (Figure 8g,h,i) are large enough to produce significantly different compositions for the same meteorite. Using the above equation, rederived for data from Dunn et al., (2010c), the Band I centers for the 25-63 μm and 125-250 μm size fractions of LL4 chondrite Soko-Banja produce Fa contents of ~29.5 mol% and ~26.73 mol% respectively. These values straddle the true measured Fa content of Soko-Banja (~28 mol%; Table 2). Comparison of Fa values measured using EPMA and predicted using the above equation in Figure 12 yields two significant observations: first, that the particle size range of a NEA can influence the deduction of its composition, and second, that the equation derived in Dunn et al. (2010c) for the silicate fraction of ordinary chondrite meteorite powders may not be applicable to ordinary chondrite powders of different grain sizes or that retain the metal fraction (more on this in Section 5.3). The Fa values predicted from the equation overestimate Fa content for the most metal-rich (H5 and H6) powders.

Changes in particle size can also mask spectral features. The ~1.3 μm absorption feature nearly disappears for a majority of the VNIR spectra of the largest size fractions of each meteorite (Figures S17-S19).

Particle size also has a strong effect on the BAR of the samples studied in this work (Figure 10). BAR generally increases as particle size increases, but does slightly decrease for the largest size fractions of the LL6, L5, and H6 samples when compared to the next largest size fraction. It is also clear that the BAR values increase across the LL, L and H chondrite groups. This is because BAR is reflective of olivine and pyroxene abundances, which decrease (olivine) and increase (pyroxene) across the H, L, and LL groups. Dunn et al. (2010c) derived an equation (Equation 4 of Dunn et al., 2010c) relating olivine and pyroxene abundance and BAR. Rederiving this equation for the Dunn et al. (2010c) band parameters calculated using the MGM method results in:

$$ol/(ol + px) = -0.312 \times BAR + 0.718 \quad (3)$$

Plugging in the BAR values of the 25-63 μm and 125-250 μm size fractions of LL4 chondrite Soko-Banja (Figure 10) yields ol/(ol+px) ratios of 0.646 and 0.578 respectively. Using the modal abundances from Table 1, Soko-Banja has an ol/(ol+px) ratio of 0.68 when the values for olivine and low-Ca pyroxene are used, and 0.63 when high-Ca pyroxene is included in the calculation with low-Ca pyroxene. It is apparent that the dependence of the BAR values on particle size results in different abundance ratios for a material of the same composition. This means that derived relationships between olivine and pyroxene abundances and BAR are not applicable to just any spectra – they must only be used for materials of the same particle size.

In summary, particle size can strongly affect compositional interpretations of multi-mineralic mixtures relevant to the interpretation of silicate-rich asteroids. In particular, the combined spectral effects of particle size and petrologic type display strong and relatively consistent trends across meteorites, and the effects of particle size, petrologic type, and metal content are important to consider when attempting to derive mineralogical compositions from VNIR spectra.

5.2 Irregularities of the L chondrites

Given the preponderance of occurrences where the L chondrites break or contradict trends observed for the LL and H chondrites, one might suspect that the properties of the L chondrites Mount Tazerzait (L5) and Suizhou (L6) used in this study are somehow irregular when compared to the LL and H chondrites. However, these L chondrites fall neatly within the mineralogical (Table 1) and compositional (Table 2) trends expected across ordinary chondrite groups and petrologic types.

Therefore, a more likely explanation for these differences is either the relatively higher porosity of Mount Tazerzait (Friedrich et al., 2014) or the potentially high shock stage of Suizhou (Xie and Chen, 2016). An increase in porosity is understood to decrease the reflectance of low and medium albedo powders (Hapke 2008). Since Mount Tazerzait has a higher bulk porosity (12.6; Friedrich et al., 2014) than Suizhou (9.5; Macke 2010), it is possible that the difference in porosity is responsible for the decreased reflectance (i.e., band minima; Figures 8e and 9e) of Mount Tazerzait. Other means of examining porosity and physical properties of sample materials at the micro-scale (e.g., nano-indentation; Moyano-Cambero et al., 2017; Grebol-Tomas et al., 2025) were not considered in this study.

Though Suizhou was initially thought to have a shock stage of S2 (very weakly shocked), Xie and Chen (2016) showed that the shock within Suizhou was highly variable and reached shock stage S6 (very strongly shocked) in some regions of the meteorite. It is therefore possible that the portion of Suizhou subsampled for this study came from a highly shocked region of the meteorite, though the subsample used was not visually distinct from the rest of the meteorite in any way (no apparent shock veins or melt pockets). The spectral consequences of shock, known as "shock darkening" (Rubin, 1992; Britt and Pieters, 1994; Lucey, 2002; Kohout et al., 2020), include decreasing band depth, an alternate explanation as to why Suizhou, the more thermally altered L chondrite, has relatively higher band minima than Mount Tazerzait (which has a very low shock stage of S1; Gattacceca et al., 2014) in Figures 8e and 9e. As discussed previously, the more altered LL and H samples have consistently smaller band minima than their less altered counterparts. Though the mechanism that causes shock darkening is not known with certainty (Kohout et al., 2020), it is understood that shock causes either mechanical deformation or high temperature diffusion which leads to disordering of crystal structures and the possible generation of nano-phase iron on/in olivine and pyroxene. The iron would presumably be sourced from the olivine or pyroxene, which would imply that shock is removing Fe from crystallographic sites and making the olivine or pyroxene lattice less FeO-rich, and therefore less absorptive. These collision-generated "opaque" phases have also been observed in carbonaceous chondrite groups (Tanbakouei et al., 2021), and have been accompanied by implanted graphitized materials in a shocked H-chondrite regolith breccia (Rubin et al. 2005a). It is worth noting that the polished thick section of Suizhou used to determine the mineral abundances and compositions in Table 1 and 2 was not the same subsample that was powdered for VNIR measurements. It is therefore possible that the piece used for EPMA analysis had a lower shock stage than the piece powdered for VNIR measurements, if the spatial scale of shock stage heterogeneity in Suizhou is small.

The L chondrites have previously been identified as breaking trends across the LL and H ordinary chondrite groups (Gaffey 1976). In particular, Gaffey (1976) observed that an argument could be made for a Band II correlation to Fs content (similar to the Band I correlation to Fa content) if the L chondrites were excluded and only the LL and H chondrites were considered. Importantly, Gaffey (1976) also noted that variation between the ordinary chondrite groups (intergroup) is less than the variation within the ordinary chondrite groups (intragroup) and suggested that "L6 chondrites are not merely equilibrated versions of the L4 and L5 chondrites, but that some systematic difference in the mineralogy exists".

5.3 Effects of Metal Content

As suggested in Section 5.1, metal content appears to affect more than just the traditionally understood parameters of absorption depth and spectral slope. Examining the specific effects of retaining the metal fraction is feasible by comparison to previous work. Dunn et al. (2010c) completed a coordinated spectral and mineralogical analysis of 48 equilibrated (types 4-6) ordinary chondrites using a single size fraction (<150 μm) and only the silicate fraction of the meteorite powder (by removing the metal fraction with a magnet).

Dunn et al. (2010c, their Fig. 2) plotted Band I center against BAR for the 48 ordinary chondrite samples evaluated in their study. Figure 13a recreates their figure and adds the four size fractions for all six meteorites examined in this study. To enable direct comparison between this work and band parameters in Dunn et al. (2010c), we acquired their original spectra from the RELAB spectral database (https://sites.brown.edu/relab/relab-spectral-database/) and derived new band parameters using the same MGM method we employed for our data.

For the Dunn et al. (2010c) samples, there is a clear delineation between and clustering of the three ordinary chondrite groups, and the Band I Center generally decreases as the BAR increases. For the samples evaluated in this work, there is also a distinct grouping of samples based on the ordinary chondrite group they belong to and a similar trend of the Band I Center decreasing as BAR increases. Differences in spectral parameter values due to particle size are apparent for the samples from this study – BAR varies strongly with particle size, petrologic type, and ordinary chondrite group type. Band I Center in Figure 13a also varies with particle size for the samples from this study, most strongly for the LL chondrite samples.

The samples from this work generally overlap the relevant sample groups from Dunn et al. (2010c) in Figure 13a. There appears to be a slight offset of the samples of this work from the samples from Dunn et al. (2010c) when comparing the two more closely in Figure 13b. Here, mean values are taken for each relevant petrologic type from each ordinary chondrite group in the Dunn et al. (2010c) data, and it is clear that there is not a 1:1 overlap between the standard deviation of the Dunn averages and the averages of related samples from this work.

There is a distinct offset observed between the silicate fraction measured in Dunn et al. (2010c) and the metal and silicate fraction measured in this work when examining Band I Asymmetry and FWHM values in Figure 13c and their averages in Figure 13d. The spectra of the samples measured in this work exhibit a markedly stronger band asymmetry than the spectra of the silicate fraction samples from Dunn et al. (2010c). The Dunn et al. (2010c) measurements were done at ambient room temperature (~20°C) on a single size fraction (<150 μm) of each meteorite. Though the measurements from this work included in Figure 13 were taken in a simulated asteroid environment chamber at a sample temperature of 10°C, one of the takeaways from Section 5.1 is that temperature effects on VNIR spectra of ordinary chondrites are minimal for the investigated temperature range. Since the particle size of the Dunn et al. (2010c) samples falls within the particle size range of the samples from this study (25-250 μm), the only

remaining fundamental difference between the Dunn et al. (2010c) investigation and this study is that Dunn et al. (2010c) used only the silicate fraction of the ordinary chondrite meteorite powders, while this study included the metal fraction along with the silicate fraction of the meteorite powders. By process of elimination, any offset between the Dunn et al. (2010c) samples and the samples in this study in Figure 13 is most likely due to the presence of the metal fraction or the fact that this work only utilized one sample per petrologic type. If the former, this means that the relatively small metal content of ordinary chondrite meteorites (~ <10% modal abundance) has a small, but non-negligible, contribution to the most common spectral features used for compositional characterization (band center, band area ratio).

This investigation adds to the body of work examining the effects of silicate and metal mixtures (Gaffey et al., 1986; Cloutis et al., 1990; Burbine et al., 2007; Lawrence and Lucey, 2007; Cloutis et al., 2015) though the majority of previous investigations have explored mixtures with much higher metal contents. That the presence of a relatively small metal fraction can so strongly influence the spectra of the relatively well-studied ordinary chondrites has serious implications for ongoing interpretations of asteroid spectra.

A notable but unlikely contributor to the variations in spectral features observed in this study is chromite. Though it has <1% abundance in the meteorites examined in this study, Cloutis et al. (2013) concluded that the presence of chromite in HED meteorites can lead to large variations in all spectral parameters. The spectrum of chromite has a strong absorption feature near 2 μm, so it is possible that this phase is contributing to the spectral character in this region. Furthermore, this work suggests that the spectral contribution of plagioclase feldspar to VNIR spectra of ordinary chondrite meteorites should be explored further, particularly if examining highly shocked samples. This phase has a modal abundance that is typically greater than that of high-Ca pyroxene (Table 1) and could be the cause of the absorption feature near 1.3 μm in the spectra in this study (cf., Gaffey 1976; Tanbakouei et al., 2021).

Finally, it is worth noting that the effects of porosity and shock are not fully explored in this study. Porosities for the samples studied here are reported in Macke (2010) and Friedrich et al. (2014), but the shock stages of three of the meteorites used in this study (Zhovtnevyi, Mangwendi, and Soko-Banja) have not been classified at the time of writing.

Overall, it is important to take care in compositional interpretations of asteroid spectra unless the surface temperature and particle size of the asteroid regolith are known. This investigation demonstrates that these physical properties can influence spectra to a degree sufficient to change compositional interpretations. The intricate interplay of temperature, particle size, petrologic type, and ordinary chondrite group type is still not fully deconvolved, and would benefit from future laboratory studies, modeling, and statistical approaches.

6 Summary and Conclusions

We measured the VNIR spectra of ordinary chondrite meteorite powders of varying grain size and petrologic type in a simulated asteroid environment, at a series of temperatures relevant to near-Earth asteroids. The sample particle sizes were consistent with the grain sizes of samples returned from the near-Earth asteroid Itokawa, which is the only asteroid thus far to have been definitively linked to an ordinary chondrite group. We find that:

1. Temperature has a minimal effect on band parameters derived from ordinary chondrite meteorite spectra. This implies that effects of temperatures in the near-Earth asteroid temperature regime (10-100ºC) on VNIR spectra are mostly negligible for olivine and

pyroxene dominated compositions. The band asymmetry and FWHM are most strongly affected by temperature, up to ±5% over 10°C to 100°C (Figures 5, 6, 7).

2. Particle size is the most critical variable to consider when trying to derive composition from remotely sensed asteroid VNIR spectra. Changes in particle size can result in variations in band centers and band area ratios for material of the same composition, two key parameters that are typically used to derive asteroid composition. Variations in particle size have a noticeable effect on predicted Fa values (Figure 12), with the strongest offset from known values observed for samples with the highest metal content. Therefore, changes in band centers and band area ratios due to particle size can mimic changes in band parameters due to composition.
3. Metal content has an overall subtle but non-trivial effect on the VNIR spectra of ordinary chondrites. Comparison with previous work examining the spectral features of the silicate fraction of ordinary chondrite powders reveals the small degree of variation in band center and BAR caused by the presence of the metal fraction, along with its connection to the effects of particle size. If particle size is unknown, metal content <10% is virtually undetectable in the band center and BAR parameters of VNIR spectra of ordinary chondrites. The threshold at which metal will "overpower" spectral variations due to particle size and become detectable is not yet known, but should be more thoroughly explored. Metal content appears to have a strong effect on band asymmetry, with the samples that contain the most metal (H chondrites) showing the largest differences in Band I asymmetry values (Figure 13c,d).
4. Changes in petrologic type of the equilibrated ordinary chondrites are correlated with a systematic change in band depth across all measured particle sizes.
5. Changes in band parameter values are not necessarily attributable to a single physical or chemical property. Band centers shift to longer wavelengths as temperature, grain size, and petrologic type increase.

In summary, these observations underscore the necessity of applying caution in compositional interpretation of remotely sensed spectra as the interplay between temperature, particle size, petrologic type, metal content, and perhaps even shock can affect spectral parameters used as diagnostics for chemical composition. Understanding how metal contributes to the spectra of multi-mineralic silicate powders is critically important for future investigations, especially missions such as such as Lucy, which will visit asteroid Psyche, thought to be metal-rich with a substantial silicate regolith component.

Acknowledgements. This research utilized spectra from Dunn et al., (2010c) acquired with the NASA RELAB facility at Brown University. The study benefitted greatly from use of the electron microprobe at the American Museum of Natural History.

Open Research

The data collected for this study are available in the American Museum of Natural History Library Digital Repository at https://hdl.handle.net/2246/6406, reference number https://doi.org/10.5531/sd.eps.10. The complete data and supplemental information are about 1 GB in size. Reviewers can temporarily find the data in Supporting Information until the DOI link is live after acceptance.

Data used for a portion of the analysis in this paper are taken from Dunn et al. (2010c). Original data used in Dunn et al. (2010c) are available via the NASA RELAB facility at Brown University (https://sites.brown.edu/relab/relab-spectral-database/).

Conflicts of Interest

The authors have no conflicts of interest to declare.

Figure Captions

Figure 1. Mg element maps of (a) Soko-Banja (LL4) and (c) Mangwendi (LL6) are on the left. Brighter areas represent higher abundances of Mg. RGB composite images (Red = Mg, Green = Ca, Blue = Fe) of (b) Soko-Banja and (d) Mangwendi are on the right. Primary mineral phases in the RGB images correspond to olivine (bright red), low-Ca pyroxene (darker red), and Fe-bearing phases (blue). Dimensions of each map are 2048 μm x 2048 μm; resolution is 4 μm/pixel.

Figure 2. a) Comparison of the relative abundances of olivine (olv) and low-Ca pyroxene (opx) determined from electron microprobe (EPMA) analysis and XRD of the 25-63 μm size fractions of each meteorite. The dashed line represents a 1:1 relationship between the EPMA and XRD ratios. b) Relative metal content of each size fraction of each meteorite, represented by the diffraction intensity of the main diffraction peak of Fe-Ni metal.

Figure 3. VNIR spectra of the 10 °C measurement of the 25-63 μm size fraction for all meteorites analyzed in this study. The spectra have been offset on the y-axis for clarity. Meteorites from the same ordinary chondrite group are paired together. In this figure, variations in the spectral shape are predominantly due to composition.

Figure 4. a) The unprocessed VNIR spectra of all size fractions of the H5 chondrite Jilin measured at 10 °C. b) The unprocessed VNIR spectra for all ten temperature measurements (10 °C – 100 °C) of the 25-63 μm size fraction of Jilin.

Figure 5. Percent difference between the various Band I parameter values for the 10 ºC and 100 ºC temperature measurements for the (a-d) 25-63 μm, (e-h) 63-90 μm, (i-l) 90-125 μm, and (m-p) 125-250 μm size fractions of all meteorites. The percent difference is calculated by subtracting the 10 ºC Band I parameter value from the 100 ºC Band I parameter value, dividing by the 10 ºC Band I parameter value, then multiplying by 100. If the calculated percent difference value is positive, that means the band parameter value has increased as temperature increased from 10 ºC to 100 ºC. If negative, then the band parameter value has decreased as temperature increased.

Figure 6. Percent difference between the various Band II parameter values for the 10ºC and 100ºC temperature measurements for the (a-d) 25-63 μm, (e-h) 63-90 μm, (i-l) 90-125 μm, and (m-p) 125-250 μm size fractions of all meteorites. The percent difference is calculated by subtracting the 10ºC Band II parameter value from the 100ºC Band II parameter value, dividing by the 10ºC Band II parameter value, then multiplying by 100. If the calculated percent

difference value is positive, that means the band parameter value has increased as temperature increased from 10ºC to 100ºC. If negative, then the band parameter value has decreased as temperature increased.

Figure 7. Percent difference between the BAR values for the 10ºC and 100ºC temperature measurements for the (a) 25-63 μm, (b) 63-90 μm, (c) 90-125 μm, and (d) 125-250 μm size fractions of all meteorites. The percent difference is calculated by subtracting the 10ºC BAR value from the 100ºC BAR value, dividing by the 10ºC BAR value, then multiplying by 100. If the calculated percent difference value is positive, that means the BAR has increased as temperature increased from 10ºC to 100ºC. If negative, then the BAR has decreased as temperature increased.

Figure 8. Calculated Band I parameter values for the 10ºC temperature measurement of all size fractions of the (a,d,g,j) LL chondrites, (b,e,h,k) L chondrites, and (c,f,i,l) H chondrites. Particle size increases across the x-axis.

Figure 9. Calculated Band II parameter values for the 10ºC temperature measurement of all size fractions of the (a,d,g,j) LL chondrites, (b,e,h,k) L chondrites, and (c,f,i,l) H chondrites. Particle size increases across the x-axis.

Figure 10. Calculated Band Area Ratio (BAR) values for the 10ºC temperature measurement of all size fractions of the a) LL chondrites, b) L chondrites, and c) H chondrites. Particle size increases across the x-axis.

Figure 11. Spectral slopes of the 10°C measurement of all size fractions of the a) LL chondrites, b) L chondrites, and c) H chondrites. Spectral slope was calculated using the short wavelength peak position of Band I and the long wavelength peak position of Band II. Colored lines represent simple linear regression models fitted to the data. The corresponding R^2 values are reported in the upper right corner of each plot. The spectral slope values for the 90-125 μm size fraction of the a) LL chondrites and the 25-63 μm size fraction of the b) L chondrites plot on top of each other.

Figure 12. Fayalite content predicted using Equation 2, plotted against Fa content measured using EPMA (values reported in Table 2). Different particle sizes are represented by different marker shapes. Variations in particle size have a noticeable effect on predicted Fa values.

Figure 13. a) Calculated Band I Center (BIC) plotted against BAR for VNIR spectra of ordinary chondrites taken from Dunn et al. (2010c) and this work. Band parameters for the Dunn et al. (2010c) data have been recalculated using the MGM method. The markers in gray represent the BIC and BAR values for the silicate fractions of the 48 ordinary chondrite meteorites measured in Dunn et al. (2010c). The different gray marker shapes represent the group (LL, L or H) that the sample belongs to. The colored markers represent the BIC and BAR values for the 10°C VNIR measurement of the ordinary chondrite samples of different particle sizes in this study. The different particle sizes are represented by different marker shapes, and the different meteorites are represented by different marker colors: Soko-Banja (light green), Mangwendi (medium green), Mount Tazerzait (light blue), Suizhou (dark blue), Jilin (magenta) and

Zhovtnevyi (dark purple). Dashed horizontal lines represent rough delineations between the ordinary chondrite groups made by Dunn et al. (2010c). b) BIC and BAR averages and associated standard deviations for each relevant petrologic type from Dunn et al. (2010c), plotted with the values for the 90-125 μm samples from this work, the most relevant size fraction to compare to the <150 μm samples used in Dunn et al. (2010c). c) Calculated Band I FWHM plotted against Band I Asymmetry for VNIR spectra of ordinary chondrites taken from Dunn et al. (2010c) and this work. d) Band I FWHM and Band I Asymmetry averages for each relevant petrologic type from Dunn et al. (2010c), plotted with the values for the 90-125 μm samples from this work.

References

Abe, M., Takagi, Y., Kitazato, K., Abe, S., Hiroi, T., Vilas, F., et al. (2006). Near-Infrared Spectral Results of Asteroid Itokawa from the Hayabusa Spacecraft. *Science*, 312(5), 1334–1338. http://doi.org/10.1126/science.1125718

Adams J. B. (1974). Visible and near-infrared diffuse reflectance spectra of pyroxenes as applied to remote sensing of solid objects in the solar system. *Journal of Geophysical Research*, 79, 4829–4836.

Adams J. B. (1975). Interpretation of visible and near-infrared diffuse reflectance spectra of pyroxenes and other rock-forming minerals. In Infrared and Raman Spectroscopy of Lunar and Terrestrial Minerals (C. I. Karr, ed.), pp. 91–116. Academic, New York.

Batchelder M. and Cressey G. (1998). Rapid, accurate quantification of clay bearing samples by X-ray diffraction whole pattern stripping. *Clays and Clay Minerals*. 46, 183–194.

Bates, H. C., King, A. J., Donaldson Hanna, K. L., Bowles, N. E., & Russell, S. S. (2020). Linking mineralogy and spectroscopy of highly aqueously altered CM and CI carbonaceous chondrites in preparation for primitive asteroid sample return. *Meteoritics & Planetary Science*, 55(1), 77–101. http://doi.org/10.1111/maps.13411

Binzel, R. P., Rivkin, A. S., Bus, S. J., Sunshine, J. M., & Burbine, T. H. (2001). MUSES-C target asteroid (25143) 1998 SF36: A reddened ordinary chondrite. *Meteoritics & Planetary Science*, 36(8), 1167–1172. http://doi.org/10.1111/j.1945-5100.2001.tb01950.x

Bland P. A., Cressey G. and Menzies O. N. (2004). Modal mineralogy of carbonaceous chondrites by X-ray diffraction and Mössbauer spectroscopy. *Meteoritics & Planetary Science*. 39, 3–16.

Bowen, B., Reddy, V., De Florio, M., Kareta, T., Pearson, N., Furfaro, R., Sharkey, B., McGraw, A., Cantillo, D., Sanchez, J. A., and Battle, A. (2023). Grain Size Effects on Visible and Near-infrared (0.35–2.5 μm) Laboratory Spectra of Ordinary Chondrite and HED Meteorites. *The Planetary Science Journal*, 4(52).

Britt, D. T. and Pieters, C. M. (1994). Darkening in black and gas-rich ordinary chondrites: The spectral effects of opaque morphology and distribution. *Geochimica et Cosmochimica Acta*, 58, 3905-3919.

Burbine, T.H., Greenwood, R.C., Buchanan, P.C., Franchi, I.A., Smith, C.L., 2007. Reflectance spectra of mesosiderites: Implications for Asteroid 4 Vesta. *Lunar and Planetary Science Conference* 38, Abstract #2119.

Burbine, T. H., Khanani, I., Kumawat, D., Hussain, A., Wallace, S. M., and Dyar, M. D. (2024) Testing the Bus-DeMeo Asteroid Taxonomy Using Meteorite Spectra. *The Planetary Science Journal*, 5(9).

Burns R. C., Huggins F. E., and Abu-Eid R. M. (1972). Polarized absorption spectra of single crystals of lunar pyroxene and olivine. *Moon*, 4, 93–102.

Burns, R. G. (1993). Mineralogical Applications of Crystal Field Theory (2nd Edition). Cambridge: Cambridge University Press, 576 pp.

Bus, S. J., and Binzel, R. P. (2002). Phase II of the Small Main-Belt Asteroid Spectroscopic Survey A Feature-Based Taxonomy. *Icarus*, 158(1), 146–177.

Cheek, L. C., Pieters, C. M., Dyar, M. D., and Milam, K. A. (2009). *Lunar and Planetary Science Conference*, 40, Abstract #1928.

Clark, R. N., and Roush, T. L. (1984). Reflectance spectroscopy: Quantitative analysis techniques for remote sensing applications. *Journal of Geophysical Research: Solid Earth*, 89(B7), 6329-6340.

Clark, R. N., Chapter 1: Spectroscopy of Rocks and Minerals, and Principles of Spectroscopy, in Manual of Remote Sensing, Volume 3, Remote Sensing for the Earth Sciences, (A.N. Rencz, ed.) John Wiley and Sons, New York, p. 3-58, 1999.

Clark B. E., Helfenstein P., Bell J. F. III, Peterson C., Ververka J., Izenberg N. I., Domingue D., Wellnitz D., and McFadden L. (2002). NEAR Infrared Spectrometer photometry of asteroid 433 Eros. *Icarus*, 155, 189–204.

Cloutis, E. A., Gaffey, M. J., Jackowski, T. L., and Reed, K. L. (1986). Calibrations of phase abundance, composition, and particle size distribution for olivine-orthopyroxene mixtures from reflectance spectra. Journal of Geophysical Research: Solid Earth, 91(B11), 11641-11653.

Cloutis, E. A., Gaffey, M. J., Smith, D. G. W., Lambert, R. St. J., (1990). Metal silicate mixtures: Spectral properties and applications to asteroid taxonomy. *Journal of Geophysical Research*, 95, 8323–8338.

Cloutis E. A. and Gaffey M. J. (1991). Pyroxene spectroscopy revisited: Spectral-compositional correlations and relationships to geothermometry. *Journal of Geophysical Research*, 91, 11641–11653.

Cloutis E. A., Izawa, M. R. M., Pompilio, L., Reddy, V., Hiesinger, H., Nathues, A., Mann, P., Le Corre, L., Palomba, E., and Bell, J. F. III. (2013). Spectral reflectance properties of HED meteorites + CM2 carbonaceous chondrites: Comparison to HED grain size and compositional variations and implications for the nature of low-albedo features on Asteroid 4 Vesta. *Icarus*, 223(2), 850-877.

Cooper D. and Mustard J., (1999). Effects of Very Fine Particle Size on Reflectance Spectra of Smectite and Palagonitic Soil. *Icarus*, 142(2), 557-570.

Crapster-Pregont, E. J. and Ebel, D. S. (2020). Reducing Supervision of Quantitative Image Analysis of Meteorite Samples. *Microscopy and Microanalysis*, 26(1), 63-75.

Cressey G. and Batchelder M. (1998) Dealing with absorption and micro absorption in quantitative phase analysis. Int. Union Crystallogr. Newslett. 20, 16–17.

DeMeo, F. E., Binzel, R. P., Slivan, S. M., and Bus, S. J. (2009). An extension of the Bus asteroid taxonomy into the near-infrared, *Icarus*, 202(1), 160–180.

DeSanctis, M. C., Ammannito, E., Capria, M. T., Capaccioni, F., Combe, J.-P., Frigeri, A., Longobardo, A., Magni, G., Marchi, S., McCord, T. B., Palomba, E., Tosi, F., Zambon, F., Carraro, F., Fonte, S., Li, Y. J., McFadden, L. A., Mittlefehldt, D. W., Pieters, C. M., Jaumann, R., Stephan, K., Raymond, C. A., and Russell, C. T. (2013). Vesta's mineralogical and composition as revealed by the visible and infrared spectrometer on Dawn. *Meteoritics & Planetary Science,* 48, 11, 2166–2184.

Dodd R. T., Van Schmus W. R., and Koffman D. M. (1967) A survey of the unequilibrated ordinary chondrites. *Geochimica et Cosmochimica Acta*, 31, 921–951.

Dodd R. T. (1969). Metamorphism of the ordinary chondrites: A review. *Geochimica et Cosmochimica Acta*, 33, 161–203.

Dunn, T. L., Cressey, G., McSween, H. Y., and McCoy, T. J. (2010a) Analysis of ordinary chondrites using powder X-ray diffraction: 1. Modal mineral abundances. *Meteoritics & Planetary Science*, 45(1), 123–134. doi:10.1111/j.1945-5100.2009.01011.x

Dunn, T. L., McSween, H. Y., McCoy, T. J., and Cressey, G. (2010b). Analysis of ordinary chondrites using powder X-ray diffraction: 2. Applications to ordinary chondrite parent-body processes. *Meteoritics & Planetary Science*, 45(1), 135–156. doi:10.1111/j.1945-5100.2009.01012.x

Dunn, T. L., McCoy, T. J., Sunshine, J. M., and McSween, H. Y. (2010c) A coordinated spectral, mineralogical, and compositional study of ordinary chondrites. *Icarus*, 208(2), 789–797.

Dyar M. D., Wallace S. M., Burbine T. H. and Sheldon, D. R. (2023). A machine learning classification of meteorite spectra applied to understanding asteroids. *Icarus* 406, 115718.

Elkins-Tanton, L. T., Asphaug, E., Bell, J. F., III, Bercovici, H., Bills, B., Binzel, R., Bottke, W. F., Dibb, S., Lawrence, D. J., Marchi, S., McCoy, T. J., Oran, R., Park, R. S., Peplowski, P. N., Polanskey, C. A., Prettyman, T. H., Russell, C. T., Schaefer, L., Weiss, B. P., Wieczorek, M. A., Williams, D. A., and Zuber, M. T. (2020). Observations, meteorites, and models: A preflight assessment of the composition and formation of (16) Psyche. *Journal of Geophysical Research: Planets*, 125, e2019JE006296

Friedrich, J. M., Rubin, A. E., Beard, S. P., Swindle, T. D., Isachsen, C. E., Rivers, M. L. and Macke, R. J. (2014). Ancient porosity preserved in ordinary chondrites: Examining shock and compaction on young asteroids. *Meteoritics & Planetary Science*, 49(7), 1214-1231.

Friedrich, J. M., Weisberg M. K., Ebel D. S., Biltz A. E., Corbett B. M., Iotzov I. V., Khan W. S., and Wolman M. D. (2015). Chondrule size and density in all meteorite groups: A compilation and evaluation of current knowledge. (invited review) *Chemie der Erde*, 172: 322-356. DOI: 10.1016/j.chemer.2014.08.003

Gastineau-Lyons, H. K., McSween, H. Y. J., & Gaffey, M. J. (2002). A critical evaluation of oxidation versus reduction during metamorphism of L and LL group chondrites, and implications for asteroid spectroscopy. *Meteoritics & Planetary Science*, 37(1), 75–89.

Gaffey, M. J. (1976). Spectral reflectance characteristics of the meteorite classes. *Journal of Geophysical Research*, 81(5), 905–920.

Gaffey, M. J. (1986). The spectral and physical properties of metal in meteorite assemblages: Implications for asteroid surface materials. *Icarus*, 66, 468-486.

Gattacceca, J., Suavet, C., Rochette, P., Weiss, B. P., Winklhofer, M., Uehara, M., and Friedrich, J. M. (2014). Metal phases in ordinary chondrites: Magnetic hysteresis properties and implications for thermal history. *Meteoritics & Planetary Science,*. **49**, 652–676.

Gemma, M. E., and Ebel, D. S. (2019). Mapping Mineral Diversity in LL Chondrites. Goldschmidt Abstracts, 2019. Abstract #1112.

Gemma, M. E. and Ebel, D. S. (2021) Mineral Abundance, Variation, and Coarsening Across Petrologic Types of H Chondrite Meteorites. *Lunar and Planetary Science Conference* 52, Abstract #2768.

Glotch, T. D., Rogers, A. D., and Hurowitz, J. A. (2016). Spectroscopy and Geochemistry Facilities at the Stony Brook University Center for Planetary Exploration. *Lunar and Planetary Science Conference*, 48, Abstract #1922.

Grebol-Tomas, P., Ibáñez-Insa, J., Trigo-Rodríguez, J. M., Peña-Asensio, E., Oliva, R., Díaz-Anichtchenko, D., Botella, P., Sánchez-Martín, J., Turnbull, R., Errandonea, D., Liang, A., Popescu, C., and Sort, J. (2025) Mechanical softening of lunar olivine probed via nanoindentation and high-pressure X-ray diffraction measurements. *Geoscience Frontiers*, 16, Issue 5, September 2025, 102110.

Greenwood, R. C., Franchi, I. A., Findlay, R., Malley, J. A., Ito, M., Yamaguchi, A., et al., (2023). Oxygen isotope evidence from Ryugu samples for early water delivery to Earth by CI chondrites. *Nature Astronomy*, 7, 29–38

Grossman, J. N., and Brearley, A. J. (2010). The onset of metamorphism in ordinary and carbonaceous chondrites. *Meteoritics & Planetary Science*, 40(1), 87-122.

Hapke, B. (1981). Bidirectional Reflectance Spectroscopy: 1. Theory. *Journal of Geophysical Research,* 86(B4), 3039-3054.

Hapke, B. (2008). Bidirectional reflectance spectroscopy 6. Effects of porosity. *Icarus,* **195**, 918–926.

Hapke, B. (2012). Theory of Reflectance and Emittance Spectroscopy (2nd ed.). Cambridge: Cambridge University Press. doi:10.1017/CBO9781139025683

Heck, P. R., Schmitz, B., Baur, H., Halliday, A. N., and Wieler, R. (2004). Fast delivery of meteorites to Earth after a major asteroid collision. *Nature*, 430, p. 323-325.

Hinrichs, J. L., P. G. Lucey, M. S. Robinson, A. Meibom, and A. N. Krot (1999). Implications of temperature-dependent near-IR spectral properties of common minerals and meteorites for remote sensing of asteroids. *Geophysical Research Letters*, 26, 1661–1664.

Hinrichs, J. L., and Lucey, P. G. (2002). Temperature-Dependent Near-Infrared Spectral Properties of Minerals, Meteorites, and Lunar Soil. *Icarus*, 155(1), 169–180.

Howard, K. T., Benedix, G. K., Bland, P. A., and Cressey, G. (2009). Modal mineralogy of CM2 chondrites by X-ray diffraction (PSD-XRD). Part 1: Total phyllosilicate abundance and the degree of aqueous alteration. *Geochimica et Cosmochimica Acta*, *73*(15), 4576-4589.

Howard, K. T., Benedix, G. K., Bland, P. A., and Cressey, G. (2011). Modal mineralogy of CM chondrites by X-ray diffraction (PSD-XRD): Part 2. Degree, nature and settings of aqueous alteration. *Geochimica et Cosmochimica Acta*, *75*(10), 2735-2751.

Huss, G. R., Rubin, A. E., and Grossman, J. N. (2006). Thermal Metamorphism in Chondrites. Meteorites and the Early Solar System II, pp. 567-586 (D.S. Lauretta and H.Y. McSween, Eds.), Univ. Arizona press.

Hutchison R. (2004) Meteorites: A Petrologic, Chemical and Isotopic Synthesis (Cambridge Univ. Press).

Ito, M., Tomioka, N., Uesugi, M. et al. (2022). A pristine record of outer Solar System materials from asteroid Ryugu's returned sample. *Nature Astronomy*, 6, 1163–1171. https://doi.org/10.1038/s41550-022-01745-5

Jarosewich E. (1990). Chemical analyses of meteorites: A compilation of stony and iron meteorite analyses. *Meteoritics*, 25, 323–337.

Johnson, J. R., and Hörz, F. (2003). Visible/near-infrared spectra of experimentally shocked plagioclase feldspars. Journal of Geophysical Research, 108, E11, 5120. doi:10.1029/2003JE002127

Jones, R. H., McCubbin, F. M., Dreeland, L., Guan, Y., Burger, P. V., and Shearer, C. K. (2014). Phosphate minerals in LL chondrites: A record of the action of fluids during metamorphism on ordinary chondrite parent bodies. *Geochimica et Cosmochimica Acta*, 132, 120-140.

1380 Kallemeyn G. W., Rubin A. E., Wang D., and Wasson J. T. (1989). Ordinary chondrites: Bulk
1381 compositions, classification, lithophile-element fractionations, and composition-petrographic
1382 type relationships. *Geochimica et Cosmochimica Acta*, 53, 2747–2767.
1383 King, A. J., Schofield, P. F., Howard, K. T., and Russell, S. S. (2015a). Modal mineralogy of CI
1384 and CI-like chondrites by X-ray diffraction. *Geochimica et Cosmochimica Acta*, 165, 148-
1385 160.
1386 Klima, R. L., Dyar, M. D., and Pieters, C. M. (2011). Near-infrared spectra of clinopyroxenes:
1387 Effects of calcium content and crystal structure. *Meteoritics & Planetary Science*, 46(3), 379-
1388 395.
1389 Kohout, T., Penttilä, A., Mann, P., Cloutis, E., Čuda, J., Filip, J., Malina, O, Reddy, V.,
1390 Grokhovsky, V. I., Yakovlev, G. A., Halodova, P., & Haloda, J. (2020). Distinguishing
1391 between Shock-darkening and Space-weathering Trends in Ordinary Chondrite Reflectance
1392 Spectra. *The Planetary Science Journal*, 1, 37.
1393 Lauretta, D. S. et al. (2022). Spacecraft sample collection and subsurface excavation of asteroid
1394 (101955) Bennu. Science, 377, 285-291. https://doi.org/10.1126/science.abm1018
1395 Lauretta, D. S., Connolly, H. C., Jr, Aebersold, J. E., Alexander, C. M. O., Ballouz, R.-L.,
1396 Barnes, J. J., Bates, H. C., Bennett, C. A., Blanche, L., Blumenfeld, E. H., Clemett, S. J.,
1397 Cody, G. D., DellaGiustina, D. N., Dworkin, J. P., Eckley, S. A., Foustoukos, D. I., Franchi,
1398 I. A., Glavin, D. P., Greenwood, R. C., Haenecour, P., Hamilton, V. E., Hill, D. H., Hiroi, T.,
1399 Ishimaru, K., Jourdan, F., Kaplan, H. H., Keller, L. P., King, A. J., Koefoed, P.,
1400 Kontogiannis, M. K., Le, L., Macke, R. J., McCoy, T. J., Milliken, R. E., Najorka, J.,
1401 Nguyen, A. N., Pajola, M., Polit, A. T., Righter, K., Roper, H. L., Russell, S. S., Ryan, A. J.,
1402 Sandford, S. A., Schofield, P. F., Schultz, C. D., Seifert, L. B., Tachibana, S., Thomas-
1403 Keprta, K. L., Thompson, M. S., Tu, V., Tusberti, F., Wang, K., Zega, T. J., Wolner, C. W.
1404 V. and the OSIRIS-REx Sample Analysis Team (2024). Asteroid (101955) Bennu in the
1405 laboratory: Properties of the sample collected by OSIRIS-REx. *Meteoritics & Planetary*
1406 *Science*. https://doi.org/10.1111/maps.14227.
1407 Lawrence, S. J. and Lucey, P. G. (2007). Radiative transfer mixing models of meteoritic
1408 assemblages. *Journal of Geophysical Research*, 112, E07005.
1409 Lucey, P. G., Keil, K., and Whitely, R. (1998). The influence of temperature on the spectra of the
1410 A-asteroids and implications for their silicate chemistry. *Journal of Geophysical Research*,
1411 103(E3), 5865–5871.
1412 Lucey, P. G., Hinrichs, J., Kelly, M., Wellnitz, D., Izenberg, N., Murchie, S., Robinson, M., Clark,
1413 B. E., and Bell, J. F. (2002). Detection of Temperature-Dependent Spectral Variation on the
1414 Asteroid Eros and New Evidence for the Presence of an Olivine-Rich Silicate Assemblage,
1415 *Icarus*, 155(1), 181–188.
1416 Lucey, P. (2002). Radiative transfer model constraints on the shock state of remotely sensed lunar
1417 anorthosites. *Geophysical Research Letters*, 29.
1418 Macke, R. J. (2010). Survey Of Meteorite Physical Properties Density, Porosity and Magnetic
1419 Susceptibility. PhD Thesis, University of Central Florida, 1638.
1420 https://stars.library.ucf.edu/etd/1638
1421 Mason B. (1963). Olivine compositions in ordinary chondrites. *Geochimica et Cosmochimica*
1422 *Acta*, 27:1011–1024.
1423 McSween H. Y., Bennett, M. E., and Jarosewich, E. (1991). The Mineralogy of Ordinary
1424 Chondrites and Implications for Asteroid Spectrophotometry. *Icarus*, 90, 107–116.

Milliken, R., Hiroi, T., Scholes, D., Slavney, S., & Arvidson, R. (2021), in Astromaterials Data Management in the Era of Sample-Return Missions Community Workshop, Abstract #2021.
Moroz, L., Schade, U., and Wäsch, R. (2000). Reflectance Spectra of Olivine–Orthopyroxene-Bearing Assemblages at Decreased Temperatures: Implications for Remote Sensing of Asteroids, *Icarus*, 147(1), 79–93.
Moyano-Cambero, C. E., Pelllilcer, E., Trigo-Rodríguez, J. M., Williams, I. P., Blum, J., Michel, P., Küppers, M., Martínez-Jiménez, M., Lloro, I., and Sort, J. (2017). Nanoindenting the Chelyabinsk meteorite to learn about impact deflection effects in asteroids. *The Astrophysical Journal*, 835, 157.
Nakamura, T., Noguchi, T., Tanaka, M., Zolensky, M. E., Kimura, M., Tsuchiyama, A., et al. (2011). Itokawa Dust Particles: A Direct Link Between S-Type Asteroids and Ordinary Chondrites. *Science*, 333(6), 1113–1116.
Okada, T., Yamamoto, Y., Inoue, T., Shirai, K., Arai, T., Ogawa, K., et al. (2006). Thermal Radiometry of Asteroid Itokawa by the XRS Onboard Hayabusa. *Lunar and Planetary Science Conference*, 37, Abstract #1965.
Okada, T., Shirai, K., Yamamoto, Y., Arai, T., Ogawa, K., Hosono, K., and Kato, M. (2006). X-ray fluorescence spectrometry of asteroid Itokawa by Hayabusa. *Science*, 312, 1338 – 1341.
Reddy V., Dunn T. L., Thomas C. A., Moskovitz N. A., and Burbine T. H. (2015) Mineralogy and surface composition of asteroids. In Asteroids IV (P. Michel et al., eds.), pp. 43–63. Univ. of Arizona Press, Tucson.
Reflectance Experiment LABoratory (RELAB) Database. [Dataset] Last accessed 1 February 2025. https://sites.brown.edu/relab/relab-spectral-database/
Roush, T. L., and Singer, R. B. (1986). Gaussian analysis of temperature effects on the reflectance spectra of mafic minerals in the 1-μm region. *Journal of Geophysical Research: Solid Earth*, 91(B), 10301–10308.
Rousseau B., De Sanctis M. C., Raponi A., Ciarniello M., Ammannito E., Frigeri A., Carrozzo F. G., Tosi F., Scarica P., Fonte S., Raymond C. A., and Russell C. T. (2021). The surface of (4) Vesta in visible light as seen by Dawn/VIR. *Astronomy & Astrophysics*, 653: A118.
Rubin A. E. (1990). Kamacite and olivine in ordinary chondrites: Intergroup and intragroup variations. *Geochimica et Cosmochimica Acta*, 54, 1217–1232.
Rubin A. E. (1992). A shock-metamorphic model for silicate darkening and compositionally variable plagioclase in CK and Ordinary chondrites. *Geochimica et Cosmochica Acta*, 56, 1705-1714.
Rubin, A. E., Trigo-Rodríguez, J. M., Kunihiro, T., Kallemeyn, G. W., and Wasson, J. T. (2005a). Carbon-rich chondritic clast PV1 from the Plainview H-chondrite regolith breccia: formation from H3 chondrite material by possible cometary impact, *Geochimica et Cosmochimica Acta*, 69(13), 3419-3430.
Rubin, A. E. (2005b). Relationships among intrinsic properties of ordinary chondrites: Oxidation state, bulk chemistry, oxygen-isotopic composition, petrologic type, and chondrule size. *Geochimica et Cosmochimica Acta*, 69(20), 4907–4918.
Sanchez, J. A., Reddy, V., Nathues, A., Cloutis, E. A., Mann, P., & Hiesinger, H. (2012). Phase reddening on near-Earth asteroids: Implications for mineralogical analysis, space weathering and taxonomic classification. *Icarus*, 220(1), 36–50.
Shepard, M. K., de Kleer, K., Cambioni, S., Taylor, P. A., Virkki, A. K., Rívera-Valentin, E. G., Sanchez-Vahamonde, C. R., Zambrano-Marin, L., F., Magri, C., Dunham, D., Moore, J., and

Camarca, M. (2021). Asteroid 16 Psyche: Shape, Features, and Global Map. *The Planetary Science Journal*, 2, 125.

Shirley, K. A., and Glotch, T. D. (2019). Particle size effects on mid-infrared spectra of lunar analog minerals in a simulated lunar environment. *Journal of Geophysical Research: Planets*, 124(4), 970-988.

Shkuratov, Y., Starukhina, L., Hoffman, H., and Arnold, G. (1999). A model of spectral albedo of particulate surfaces: Implications for optical properties of the Moon. *Icarus*, 137, 235-246.

Singer, R. B. (1981). Near-infrared spectral reflectance of mineral mixtures: Systematic combinations of pyroxenes, olivine, and iron oxides. *Journal of Geophysical Research*, 86, 7967-7982.

Singer, R. B., and Roush, T. L. (1985). Effects of temperature on remotely sensed mineral absorption features. *Journal of Geophysical Research*, 90(B14), 12434-12444.

Sunshine, J. M., and Pieters, C. M. (1993). Estimating modal abundances from the spectra of natural and laboratory pyroxene mixtures using the modified Gaussian model. *Journal of Geophysical Research*, 98(E5), 9075–9087. http://doi.org/10.1029/93JE00677

Sunshine, J. M., & Pieters, C. M. (1998). Determining the composition of olivine from reflectance spectroscopy. *Journal of Geophysical Research*, 103(E6), 13675–13688.

Takir, D., Reddy, V., Sanchez, J. A., Shepard, M. K., and Emery, J. P. (2017). Detection of water and/or hydroxyl on asteroid 16 Psyche. *The Astronomical Journal*, 153, 31.

Tanbakouei, S., Trigo-Rodríguez, J. M., Llorca, J., Moyano-Cambero, C. E., Williams, I. P., and Rivkin, A. S. (2021). The Reflectance Spectra of CV-CK Carbonaceous chondrites from the Near Infrared to the Visible, *Monthly Notices of the Royal Astronomical Society*, 507, 651-662.

Trombka, J. I., Squyres, S. W., Brückner, J., Boynton, W. V., Reedy, R. C., McCoy, T. J., et al. (2000). The Elemental Composition of Asteroid 433 Eros: Results of the NEAR-Shoemaker X-ray Spectrometer. *Science*, 289(5), 2101–2105.

Tsuchiyama, A., Uesugi, M., Matsushima, T., Michikami, T., Kadono, T., Nakamura, T., et al. (2011). Three-Dimensional Structure of Hayabusa Samples: Origin and Evolution of Itokawa Regolith. *Science*, 333(6), 1125–1128. http://doi.org/10.1126/science.1207807

Urey, H. C. and Craig, H. (1953). The composition of the stone meteorites and the origin of the meteorites. *Geochimica et Cosmochimica Acta*, 4, 36-82.

Van Schmus W. R. and Wood J. A. (1967). A chemical-petrologic classification for the chondritic meteorites. *Geochimica et Cosmochimica Acta*, 31, 747–765.

Vernazza, P., Binzel, R., Thomas, C., DeMeo, F. E., Bus, S. J., Rivkin, A. S., and Tokunaga, A. T. (2008). Compositional differences between meteorites and near-Earth asteroids. *Nature* 454, 858–860. https://doi.org/10.1038/nature07154

Weisberg, M.K., McCoy, T.J., and Krot, A.N., (2006). Systematics and Evaluation of Meteorite Classification. Meteorites and the Early Solar System II, pp. 19-52 (D.S. Lauretta and H.Y. McSween, Eds.), Univ. Arizona press.

Xie, X. and Chen, M. (2016). Suizhou Meteorite: Mineralogy and Shock Metamorphism. (Springer-Verlag Berlin Heidelberg, 2016).

Yokoyama, T. et al., (2023). Samples returned from the asteroid Ryugu are similar to Ivuna-type carbonaceous meteorites. *Science* 379, eabn7850. DOI:10.1126/science.abn7850

[1]http://davinci.asu.edu/index.php?title=Main_Page